



Escola Tècnica Superior d'Enginyeries
Industrial i Aeronàutica de Terrassa

UNIVERSITAT POLITÈCNICA DE CATALUNYA

*Study for the numerical resolution of conservation equations
of mass, momentum and energy to be applied on vortex-
induced vibrations of cylindrical structures*

Report

Final Degree Project

Author: Albert Vega Valeri

Director: Dr. Carlos David Pérez Segarra

Co-Director: Dr. Francesc Xavier Trias Miquel

Grau en Enginyeria en Tecnologies Aeroespacials

Escola Tècnica Superior d'Enginyeries Industrial i Aeronàutica de Terrassa

Universitat Politècnica de Catalunya

Terrassa - Juny de 2015

Abstract

The main aim of this work is to be an introduction to the development of numerical codes for fluid dynamics and make them capable of represent real situations with academic purposes. Starting from a very basic point, the Navier-Stokes equations are discretized following a finite volume methodology. Then the self-developed codes are verified using different techniques and comparing the obtained results to benchmark solutions. Finally, the software is used to study a more specific case related with engineering.

Agraïments

Voldria començar aquest document reconeixent a totes aquelles persones que han col·laborat d'una manera o altra en la realització d'aquest Treball de Final de Grau ja que sense elles això no hagués estat possible.

En primer lloc agrair al doctor Carlos D. Pérez Segarra i al doctor Assensi Oliva la passió que transmeten a les seves classes, fet que sens dubte ha tingut una gran influència en que m'interessés per la dinàmica de fluids computacional. També recordar que van ser ells els que em van animar a fer el treball en aquest àmbit i van acceptar de portar-lo.

També agrair de manera especial l'ajuda prestada pel doctor Francesc Xavier Trias que ha permès superar les dificultats que s'han anat presentant i aconseguir que els codis desenvolupats funcionessin tal com és degut.

Per altra banda, aquest treball significa el final d'un cicle i és, en part, un reflex de tot lo après durant aquests darrers quatre anys que evidentment ha estat possible gràcies a tots els professors de l'Escola Superior d'Enginyeries Industrial i Aeronàutica de Terrassa.

Per últim, però no menys important, un especial agraïment per totes aquelles persones properes, companys, família i amics pel seu suport incondicional i anímic que és indispensable.

List of contents

1	Introduction	11
1.1	<i>Aim</i>	11
1.2	<i>Scope</i>	11
1.3	<i>Requirements</i>	11
1.4	<i>Justification</i>	12
1.5	<i>Brief history</i>	13
1.6	<i>State of the art</i>	15
2	Mathematical background	17
2.1	<i>Governing equations for fluid dynamics</i>	17
2.1.1	Continuity equation	17
2.1.2	Momentum equation	17
2.1.3	Energy equation	18
2.1.4	Coupled partial differential equations	19
2.2	<i>Numerical methods</i>	20
2.2.1	Finite volume method	20
2.2.2	Numerical schemes	20
2.2.3	Fractional step method	24
2.2.4	Mesh	25
2.2.5	Solvers	28
3	Code verification	33
3.1	<i>Method of manufactured solutions</i>	33
3.1.1	Diffusive term	34
3.1.2	Convective term	35
3.2	<i>Smith-Hutton problem</i>	36
3.2.1	Governing equations and boundary conditions	36
3.2.2	Numerical method	37
3.2.3	Results	37
3.3	<i>Driven cavity problem</i>	41
3.3.1	Governing equations and parameters	41
3.3.2	Boundary conditions	41
3.3.3	Numerical method	42
3.3.4	Results	44
3.4	<i>Differentially heated cavity</i>	52
3.4.1	Governing equations and parameters	52
3.4.2	Boundary conditions	53

3.4.3	Numerical method	54
3.4.4	Results.....	55
4	Vortex-induced vibrations.....	61
4.1	<i>Definition of the phenomena</i>	61
4.2	<i>Governing equations and numerical method</i>	63
4.2.1	Governing equations	63
4.2.2	Numerical method	64
4.3	<i>Geometry and boundary conditions</i>	65
4.3.1	Mesh and geometry.....	65
4.3.2	Boundary conditions.....	66
4.4	<i>Results</i>	68
4.4.1	Steady flow	68
4.4.2	Unsteady flow	70
4.4.3	Commentary on the obtained results.....	74
5	Conclusions and future lines.....	75
5.1	<i>Conclusions</i>	75
5.2	<i>Future lines</i>	76
5.3	<i>Environmental impact</i>	76
References	77

List of figures

FIGURE 2.1: A FINITE VOLUME, IN GREY, WITH ITS GEOMETRICAL ELEMENTS AND NEIGHBORS.....	21
FIGURE 2.2: EXAMPLES OF STRUCTURED AND UNSTRUCTURED MESH. EXTRACTED FROM: [11]	26
FIGURE 2.3: STRUCTURED UNIFORM MESH AND STRUCTURED NON-UNIFORM MESH	27
FIGURE 2.4: STAGGERED MESH USED TO CALCULATE THE DIFFUSIVE TERM	28
FIGURE 3.1: ERROR NORM VERSUS ELEMENT SIZE FOR THE DIFFUSIVE TERM	34
FIGURE 3.2: ERROR NORM VERSUS ELEMENT SIZE FOR THE CONVECTIVE TERM.....	35
FIGURE 3.3: REPRESENTATION OF THE DOMAIN AND THE FLOW FOR THE SMITH-HUTTON PROBLEM.....	36
FIGURE 3.4: OUTLET DISTRIBUTION FOR $P/\Gamma = 1E3$ WITH DIFFERENT MESH SIZES.....	38
FIGURE 3.5: OUTLET DISTRIBUTION FOR $P/\Gamma = 1E6$ WITH DIFFERENT MESH SIZES.....	39
FIGURE 3.6: ERROR NORM VERSUS ELEMENT SIZE FOR DIFFERENT CASES AND NUMERICAL SCHEMES...	39
FIGURE 3.7: CENTERLINE VELOCITIES COMPARISON AT $Re = 100$	45
FIGURE 3.8: CENTERLINE VELOCITIES COMPARISON AT $Re = 400$	45
FIGURE 3.9: CENTERLINE VELOCITIES COMPARISON AT $Re = 1.000$	46
FIGURE 3.10: CENTERLINE VELOCITIES COMPARISON AT $Re = 3.200$	46
FIGURE 3.11: CENTERLINE VELOCITIES COMPARISON AT $Re = 5.000$	47
FIGURE 3.12: CENTERLINE VELOCITIES COMPARISON AT $Re = 7.500$	47
FIGURE 3.13: CENTERLINE VELOCITIES COMPARISON AT $Re = 10.000$	48
FIGURE 3.14: CENTERLINE VELOCITIES COMPARISON AT $Re = 10.000$ USING A DENSER MESH	48
FIGURE 3.15: STREAMLINES FOR $Re=100$	50
FIGURE 3.16: STREAMLINES FOR $Re=1.000$	50
FIGURE 3.17: STREAMLINES FOR $Re=10.000$	51
FIGURE 3.18: REPRESENTATION OF THE DOMAIN. EXTRACTED FROM [23]	54
FIGURE 3.19: NUMERICAL ERROR OF Nu_0 VERSUS ELEMENT SIZE.....	58
FIGURE 3.20: STREAMLINES AND ISOTHERMS FOR $Ra=1E3$	59
FIGURE 3.21: STREAMLINES AND ISOTHERMS FOR $Ra=1E4$	59
FIGURE 3.22: STREAMLINES AND ISOTHERMS FOR $Ra=1E5$	60
FIGURE 3.23: STREAMLINES AND ISOTHERMS FOR $Ra=1E6$	60
FIGURE 4.1: GRAPHIC REPRESENTATION OF THE DOMAIN AND THE OBSTACLE. EXTRACTED FROM: [27]	65
FIGURE 4.2: EXAMPLE OF THE MESH USED IN THE SIMULATIONS.	66
FIGURE 4.3 STREAMLINES AROUND THE CYLINDER FOR DIFFERENT Re NUMBERS.	68
FIGURE 4.4: DIMENSIONLESS RECIRCULATION LENGTH VS. REYNOLDS NUMBER	69
FIGURE 4.5 C_d VS Re FOR STEADY REGIMES	69
FIGURE 4.6: STREAMLINES FOR $Re=60$ AT $T=584s$ AND $T=100s$	70
FIGURE 4.7: STREAMLINES FOR $Re=150$ AT $T=100s$ AND $T=236s$	70
FIGURE 4.8: DOWNSTREAM VORTEX VISUALIZATION FOR $Re=100$	71
FIGURE 4.9: PERIODIC BEHAVIOR OF THE AERODYNAMIC COEFFICIENTS FOR $Re = 100$	71
FIGURE 4.10: TIME AVERAGED DRAG COEFFICIENT VS. REYNOLDS NUMBER.....	72
FIGURE 4.11: LIFT VARIATION VS. REYNOLDS NUMBER.....	73
FIGURE 4.12: DRAG VARIATION VS. REYNOLDS NUMBER.....	73
FIGURE 4.13: STROUHAL VS. REYNOLDS NUMBER.....	74

List of tables

TABLE 3.1: RESULTS COMPARISON OF THE SOLUTION OBTAINED USING A 400x200 ELEMENT MESH.....	37
TABLE 3.2: RESULTS COMPARISON FOR $RA=1E3$	56
TABLE 3.3: RESULTS COMPARISON FOR $RA=1E4$	56
TABLE 3.4: RESULTS COMPARISON FOR $RA=1E5$	57
TABLE 3.5: RESULTS COMPARISON FOR $RA=1E6$	57

1 Introduction

1.1 Aim

The aim of this study is to understand the physics behind the fluid dynamics and heat transfer as well as develop, validate and verify self-developed software for computational fluid dynamics (CFD) and heat transfer (HT).

1.2 Scope

The scope of this study is stated as follows:

- Brief introduction to the history and evolution of CFD as well as a review of the actual techniques (State-of-the-art).
- Introduction to the finite volume methods techniques as well as the mathematical and numerical background required for solving the Navier-Stokes equations.
- Development of software capable of solving the Navier-Stokes equations (mass, momentum and energy) for 2D incompressible laminar flows, with the option to extent the field of study to incompressible turbulent flows if it is viable
- Preliminary study of a particular case chosen according to the inherent limitations of the developed codes and the available resources and future planning development.

1.3 Requirements

This study will have some requirements in order to meet properly meet the aim and the scope as well as to achieve the final goals. They are stated as follows:

- Every studied case must have the proper mathematic background specified either in the references or in the final document.
- The codes must be written in C++ language and compile in different systems.
- The codes must be tested using benchmark cases in order to determine if they are enough accurate and modified if some drawbacks are found.
- The software will be executed in personal computers so the field of study may be restricted and also some simplifications might be applied if it is possible.

1.4 Justification

Since the Navier-Stokes equations were derived by Claude-Louis Navier and George Gabriel Stokes in the 19th century, the scientific community has continuously tried to find a solution for these set of partial differential equations. The research is justified because they can be used to describe the physics of a wide range of fields with scientific or engineering interest.

The problem comes when these equations do not have a general solution and they cannot be solved analytically. In many cases, numerical methods are the only approach that can be used to approximate the solution of the Navier-Stokes equations.

However, using only numerical analysis is not enough. The methodology used for CFD calculations was known in the firsts decades of the 20th century but the nature of fluxes is so complex that the computation power required to solve the equations was not available at that time so it was impossible to achieve solutions. The use of computers is compulsory and that's the reason why the progresses achieved in this field are closely bounded to evolution of the computers and processors capabilities.

CFD techniques have become more popular in the recent years because the actual computers are fast enough to obtain results that were unimaginable some years ago and permit engineers and companies to avoid the high costs of using experimental wind tunnels and other experiments, that otherwise have also their own limitations.

The development of software capable of solving these crucial equations leads to a better understanding of the physics beyond the fluid dynamics and the possibility to develop new technologies and products using this powerful tool.

It is true that nothing can predict a more realistic behaviour than the real world itself, but it is also certain that is very difficult to recreate the exact conditions in a laboratory or in a wind tunnel. Even though you can do it, you will have to deal with sensor's precision and having information in a very few points. Using a CFD simulation avoids the need of building different prototypes and permits to obtain the solution and see the results in the whole domain for each time-step.

Furthermore, using self-developed codes gives the opportunity to optimize and adapt the solvers to very specific cases and obtain better and faster solutions rather than using commercial available software, with their expensive licenses.

Following the recent years tendency, computational fluid dynamics is going to be the future of the study of fluid dynamics. This project tries to be a first approach to this fascinating world.

1.5 Brief history

Fluid mechanics is the branch of physics that is focused on the study of fluids, their behaviour and the forces that act on them. At the same time, this discipline can be divided into fluid statics and fluid dynamics, the first one centred on fluids at rest and the second on their motion.

The study of fluids was initiated in the ancient Greece when Archimedes developed his work on fluid statics and the measurement of volumes and densities. This was the first rational and mathematical approach to a phenomenon that had fascinated humans since the appearance of the firsts civilizations. The investigations carried out by Greek physicists set the basis of this discipline that was mastered by Romans and their interest on water infrastructures like aqueducts, harbours and canals. [1]

After the hard centuries for science during the middle age, the Renaissance brought, among other things, a new perspective for science and a new generation of scientists that recovered the interest of the ancient civilizations for the study of fluids. The observations and the inventions of Leonardo Da Vinci were followed in the 17th century for Isaac Newton studies. The contributions of the English physicist and mathematician were large and important: his second law, the concept of Newtonian viscosity and the reciprocity principle that related the force that appear on an object into a stream with the change in momentum of the fluid.

During the 18th and 19th century, the efforts were focused on the mathematical description of the behaviour of fluids and its motion. Each step tried to get close to reality adding more complexity into the models. Daniel Bernoulli presented his famous principle in 1738 and Leonhard Euler proposed the Euler equations that were valid for inviscid fluids. Years later, Claude Louis Navier and George Gabriel Stokes introduced viscous transport to Euler equations and derived the well-known Navier-Stokes equations for the conservation of mass, momentum, pressure, species and turbulence. This set of partial differential equations proposed nearly 200 years ago still remain as the basis of the modern fluid dynamics and are the main focus of interest for research in this field, part for its power and ability to describe the motion of fluids and part for its complexity and the fact that they do not have analytical solution. [2]

The Navier-Stokes equations are so closely coupled that were impossible to solve with the technology available at that time. This impediment supposed a shift on the field of study and a lot of work was done on refining theories of boundary layers and turbulence in fluid flow. Ludwig Prandtl, Osborne Reynolds, Theodore von Karman or Andrey Nikolaevich Kolmogorov works and discoveries were of great importance on the field.

During the first decades of the 20th century, the development of closed form analytical solutions for particular cases reached a highly mature stage and researchers begin to be aware that with this approach many problems would remain unsolved. [3] This resulted in the development of semi-analytical techniques and numerical solution procedures. In that way, the works of Walter Ritz, Richard Courant, Kurt Friedrichs and Hans Lewy were of crucial importance to demonstrate the existence of numerical solution for the Navier-Stokes equations and for the development of finite element and finite difference methods as well as explicit schemes.

In the middle of the 20th century Lewis Fry Richardson proposed the first numerical weather prediction system using finite difference approximations and dividing the physical space into grid cells, but soon he realized that the enormous amount of calculation required by his model could not be carried out by a single person. He spent six weeks calculating an eight-hour prediction and his intend ended in failure. Also, in Japan, M. Kawaguti followed a similar approach to calculate the flow around a cylinder using a mechanical calculator and working 20 hours a week for 18 months.

The advent of digital computers supposed a solution, and a revolution, as they could be used to do the enormous calculation procedure: computational fluid dynamics was born. [4]

In the 1960s, the first simulations using computers were done. The theoretical division of NASA at Los Alamos was key for the development of new numerical methods that are still in use today such as Particle-in-Cell (PIC) or Marker-and-Cell (MAC). [5] Another important event for the evolution of CFD was the publishing of the book "Numerical Heat Transfer and Fluid Flow" by Suhas V. Patankar and the previous development of the well-known algorithm SIMPLE and their later improvements SIMPLER and SIMPLEC together with Brian Spalding. This work is considered pioneering for the development of the commercial CFD codes that bring those powerful tools to industry and their application into the design of new products in many fields. [3]

However, these examples are only a little part of the codes and methods developed during the last decades of the 20th century. Universities, engineering companies and even governmental agencies all over the world saw the great potential of these techniques and the fact that its field of application was very wide. A lot of resources were spent developing more accurate methods, each one capable to cope with more difficult problems and also improving the mathematical models used to simulate an extended range of situations.

CFD codes are still experimenting a continuous evolution and are a big focus of interest for scientific research. Year after year they are more reliable and in conjunction with high-speed supercomputers, their possibilities increase.

1.6 State of the art

The importance of numerical simulations has become so vital that this subject has created its own place between analytical solutions and experimentation in every engineering project.

Engineers have the possibility to substitute expensive wind tunnel measurements and prototypes with the use of computers. It is certain that even the best simulation done in the more powerful computer imagined cannot represent reality without any kind of error, but CFD brings an interesting alternative. For example a numerical simulation gives the flow conditions in the whole domain when the measurements in a wind tunnel can only be done in very few points. Another possibility is to test extreme conditions that would be very difficult to represent experimentally. Very large sizes, fast transients or very high temperatures can be simulated with some degree of confidence. [3]

These possibilities are changing the way engineers work, especially in the fields of fluid dynamics and combustions. Many aerospace companies perform the preliminary and a large part of the design process of their components using CFD simulations leaving wind tunnel experiments to validate the results and do the final and fine tuning adjustments. [3]

The evolution of CFD has been closely related with the evolution of computers and their capacity and the power of today's supercomputers is amazing. Nevertheless, the phenomenon studied is so complex that they are still a limitation.

One of the biggest challenges of CFD is that the different variables have to be calculated in a discrete domain rather than a continuous one. This is due to the fact that the real world is *continuous* but is impossible to study a domain of *infinite* points. The solution is to discretise the real domain in a certain number of points, as many as possible to get good accuracy. To do so, the most advanced numerical codes use high-order numerical approximations to evaluate the variables at these discrete points. This means that a variable is evaluated in a certain discrete point using the information of neighbouring discrete points. The approximation is more accurate when more points are used and also the order of the numerical scheme.

Another problem for researchers is the reproduction of what happens in very small scales. The effects of turbulence or combustion occur in very short distances and at a very high speed. Navier-Stokes equations are known to be able to represent all turbulent flows if the grid used is refined enough. This means that the numerical solution would be able to capture every little variation and the flow. Furthermore, due to the unsteady nature of these flows, the conditions have to be simulated a lot of times per second and things get worse as more turbulent the flow is.

Millions of control volumes have to be solved thousands of times every second. This approach is known as DNS (direct numerical simulation) and, as can be imagined, its computational cost is huge. It is estimated that the power needed for DNS simulations is proportional to the Reynolds number at the power of three.

To avoid this limitation, turbulence models are used. The mission of these models is to resolve only a part of the turbulent scales (the bigger ones) while the others are estimated, or modelled. Different models have been proposed like RANS models (Reynolds Averaged Navier Stokes), LES models (large eddy simulation) or DES models (detached eddy simulation). The computational cost of these models would depend on the range of scales that are directly resolved, but they are far cheaper than pure DNS. [5]

Commercial CFD codes also use some of these approaches to simulate flow conditions depending on the developers' choice. Although the first available versions of these codes were not very reliable and hard to use, their evolution has been noticeable since its appearance in the middle 80's and nowadays they are a great option for companies when qualified technicians use them. However, commercial codes are rarely used in state-of-the-art research due to accuracy limitations, the limited access that the user has to the solution methodology and lack of options to modify the code if needed. [3]

For all these reasons and its usefulness, computational fluid dynamics has emerged as a very important discipline and the predictions show that its impact would take more importance in forthcoming years in different fields of science and engineering.

2 Mathematical background

The aim of this study is to develop software capable of solving the equations that describe complex natural phenomena like heat transfer and fluid dynamics. The starting point must be the analysis of these equations that is detailed in the following pages.

2.1 Governing equations for fluid dynamics

Talking about a mathematical approach to fluid dynamics means to talk about Navier-Stokes equations. They are a set of differential equations that describe the motion of viscous fluid substances through the application of different conservation principles. Taking a control volume filled with a fluid and the continuum of matter assumption, which is believed to be extremely accurate for most macroscopic phenomena, the derivation of the equations is based on three basic principles, which are treated separately in the following lines, and the application of the transport theorem. For detailed explanation on the derivation of the equations, refer to [6].

2.1.1 Continuity equation

The equation of continuity stands on the principle that mass is neither created nor destroyed. The representation of this principle, considering an inertial frame of reference, leads to the following equation that is presented in its differential form

$$\frac{\partial \rho}{\partial t} + \nabla \cdot (\rho \mathbf{u}) = 0 \quad (2.1)$$

Where ρ is the density of the fluid, \mathbf{u} is the velocity vector with its different components and $\nabla \cdot$ is the vector operator divergence.

For further simplification, ρ will be considered constant along the whole temporal and physical domain and the continuity equation for incompressible flows stands as

$$\nabla \cdot \mathbf{u} = 0 \quad (2.2)$$

2.1.2 Momentum equation

Conservation of momentum relays on Newton's second law, expressing that the rate of change of momentum of a portion of the fluid equals to the force applied to it. Taking into account only gravitational body forces, the equation is presented also in its differential form

$$\frac{\partial(\rho \mathbf{u})}{\partial t} = -\nabla \cdot (\rho \mathbf{u}) \mathbf{u} - \nabla p + \nabla \cdot \boldsymbol{\tau} + \rho \mathbf{b} \quad (2.3)$$

ρ is the density of the fluid, \mathbf{u} the velocity vector, p the pressure, $\boldsymbol{\tau}$ the stress tensor and \mathbf{b} the vector of body forces.

Besides the assumption of incompressibility that was already made for the continuity equation, in the case of the momentum equation some other simplifications will be made to reduce the complexity of its resolution.

On one hand, to simplify the body forces term, electromagnetic forces will be neglected leaving the gravitational force as the only one taken into account. The Boussinesq hypothesis, which consider constant physical properties everywhere but in the body forces term, will be also applied in natural convection cases.

On the other hand, the stress tensor could be simplified considering Newtonian fluids. In a fluid of this kind, the viscous stresses are proportional to the gradient of the velocity and the values of the different components of the tensor can be obtained from it. Considering incompressible flows and constant viscosity (for an arbitrary coordinate system)

$$\tau_{ij} = \mu \left(\frac{\partial v_i}{\partial x_j} + \frac{\partial v_j}{\partial x_i} \right) \quad (2.4)$$

Where μ is the viscosity of the fluid, v_i refers to the velocity component parallel to the i axis and x_j the j^{th} spatial coordinate.

With all that considerations, the final form of the momentum equation is

$$\frac{\partial \mathbf{u}}{\partial t} + (\mathbf{u} \cdot \nabla) \mathbf{u} = -\nabla p' + \nu \Delta \mathbf{u} + \mathbf{g} \quad (2.5)$$

Where $\nu = \mu/\rho$ is the kinematic viscosity, $p' = p/\rho$, \mathbf{g} is the gravity acceleration vector and Δ is the Laplacian or Laplace operator.

2.1.3 Energy equation

Conservation of energy stays on that energy is nor created neither destroyed. The energy of a fluid can be split in two kinds, the kinetic energy related with the movement of the fluid and the internal energy, which can not be seen in macroscopic scale but is related with intermolecular potentials and molecular vibrations. Applying the transport theorem, the derived energy equation is

$$\rho \left(\frac{Du}{Dt} + \frac{De_k}{Dt} \right) = \nabla \cdot (\lambda \nabla T) - \nabla \cdot \mathbf{q} - \nabla \cdot (p\mathbf{u}) + \nabla \cdot (\mathbf{u} \cdot \boldsymbol{\tau}) + \rho \mathbf{u} \cdot \mathbf{g} \quad (2.6)$$

Where u is the internal energy, e_k is the kinetic energy, λ the thermal conductivity of the fluid, T the temperature and \mathbf{q} the heat flow.

In order to avoid dealing with complex thermodynamic aspects, other simplifications will be added to the previous ones. Fluids will be treated as perfect gases with the internal energy, u , as function of temperature and constant specific heat, c_p

$$du = c_p dT \quad (2.7)$$

Neglecting viscous dissipation of heat and compression or expansion work and considering non-participating medium in radiation as well as mono-component and mono-phase fluid, the simplified energy equation obtained is

$$\frac{\partial T}{\partial t} + \mathbf{u} \cdot \nabla T = \frac{\lambda}{\rho c_p} \Delta \mathbf{u} + \frac{\Phi}{\rho c_p} \quad (2.8)$$

Where Δ is the Laplace operator and Φ represents a heat source.

2.1.4 Coupled partial differential equations

Now that the different equations for fluid dynamics have been presented, the problem that arises is the existence of a strong coupling between them. The unknowns are the components of the velocity, the pressure and the temperature and the coupling exist in two ways.

For incompressible flows, there is a coupling between pressure and velocity. As there is no specific equation for pressure, the pressure field is the one that makes the velocity accomplish the mass conservation equation.

Another coupling exists between temperature and velocity but only under determined circumstances. If physical properties are considered constant, the velocity field does not depend on the temperature. However, in natural convection, where at least Boussinesq hypothesis must be taken into account, or more general cases with temperature dependant physical properties, velocity and temperature fields are dependant on each other.

The existence of these couplings add another difficulty on the process of solving fluid dynamics equations and investigators are forced to use different strategies to overcome this problem. Some of them will be showed in the following chapters.

2.2 Numerical methods

In the previous parts, the governing equations of the field of study have been presented. The result was a set of complex coupled partial differential equations that has to be solved in order to study the physical phenomena. However, due to its characteristics, there is not analytical solution for these equations.

Numerical methods use different techniques and approximations to provide a discrete solution for the distribution of a certain physical property. There are different approaches that can be followed to obtain a numerical solution and the one used in this study is explained in the following pages.

2.2.1 Finite volume method

The finite volume method is similar to the finite difference method or the finite element method. All of these methods are used to represent and evaluate partial differential equations in the form of algebraic equations, which implies that the different variables are calculated at discrete points on a meshed geometry. *Finite volume* stands for a very small volume that surrounds each mesh point, creating a grid of cells along the whole domain.

The use of very small *finite volumes* is the main difference between this method and the others. Unlike classical finite methods, where derivatives are approximated by finite differences, the finite volume method converts volume integrals in the differential equations into surface integrals using the divergence theorem. Then, the fluxes across the surfaces of the control volumes are approximated and the integral is evaluated over each cell. As the physical quantity is evaluated as an average along each cell, the finite volume method offers a great advantage when the function presents some discontinuities and the finite differences cannot evaluate the function properly. [7]

In this kind of method, the flux entering a given volume is identical to the one leaving the adjacent volume. This means that the method is conservative as cell averages change through the edge fluxes. Another advantage of the finite volume method is that it is very easy to implement to unstructured meshes.

2.2.2 Numerical schemes

As it has been explained before, the finite volume method will transform the partial differential equations that govern fluid dynamics or heat transfer into a system of algebraic equations much more easy to solve with the help of a computer. However, the continuous equations have to be discretized, both in time and space, to obtain the desired system of algebraic equations.

2.2.2.1 Spatial discretization

All the equations presented in section 2.1 have a similar structure that can be summarized in the following convection diffusion equation [8]

$$\frac{\partial \rho \phi}{\partial t} + \nabla(\rho \mathbf{u} \phi) = \nabla(\Gamma \nabla \phi) + S \quad (2.9)$$

Where ϕ is the physical quantity that is being transported, ρ the density, \mathbf{u} the velocity vector, Γ the diffusion coefficient and S the source term. The two terms that appear in the left hand side are, respectively, the temporal variation and the convective term and the right hand side is formed by the diffusive and source terms.

Applying the Gauss theorem, the integral of volume can be converted into an integral of the fluxes across the surface of the volume. For the convective and diffusive terms

$$diff = \int_{\Omega} \nabla(\Gamma \nabla \phi) d\Omega = \int_{\partial\Omega} \Gamma \nabla \phi \cdot \mathbf{n} dS \quad (2.10)$$

$$conv = \int_{\Omega} \nabla(\rho \mathbf{u} \phi) d\Omega = \int_{\partial\Omega} (\rho \mathbf{u}) \phi \cdot \mathbf{n} dS \quad (2.11)$$

Then, integrating the transformed equation into a rectangular 2D control volume (leaving for a moment the transient term that will be treated later)

$$\begin{aligned} \frac{\partial \rho \phi}{\partial t} + [(\rho u \phi)_e - (\rho u \phi)_w] \Delta y + [(\rho v \phi)_n - (\rho v \phi)_s] \Delta x &= \\ = \left[\left(\Gamma \frac{\partial \phi}{\partial x} \right)_e - \left(\Gamma \frac{\partial \phi}{\partial x} \right)_w \right] \Delta y + \left[\left(\Gamma \frac{\partial \phi}{\partial y} \right)_n - \left(\Gamma \frac{\partial \phi}{\partial y} \right)_s \right] \Delta x + S \Delta x \Delta y & \end{aligned} \quad (2.12)$$

Where the different parameters can be seen in the following image

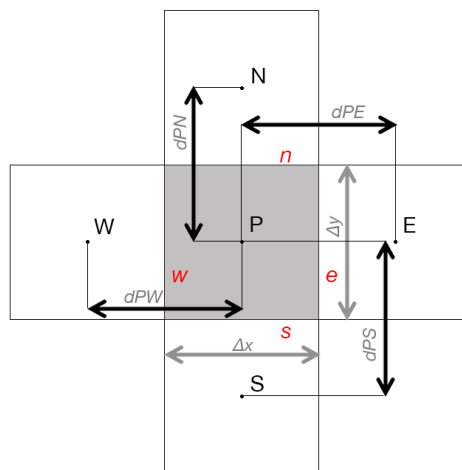


Figure 2.1: A finite volume, in grey, with its geometrical elements and neighbours

From equation 2.12 it can be seen that both the derivatives and the physical quantities are evaluated in the faces of the control volume. However, the node is placed in the centre of the volume so the dependent variable is calculated there. There is a need to find some way to evaluate the values at the faces.

Derivatives are calculated as an arithmetic mean. Notice that capital letters refer to the neighbour nodes (East, West, North and South) whereas lowercases refer to the surfaces

$$\left(\frac{\partial \phi}{\partial x}\right)_e = \frac{\phi_E - \phi_P}{\delta x_{ep}} \text{ or } \left(\frac{\partial \phi}{\partial y}\right)_n = \frac{\phi_N - \phi_P}{\delta y_{np}} \quad (2.13)$$

The evaluation of the variable at the faces of the control volume is carried out by the numerical scheme.

There are different numerical schemes. One of the most important characteristics of the numerical scheme is the *order* or in other words the number of neighbouring nodes that are used to evaluate the variable at the cell face.

In this study, two different low-order numerical schemes are used:

- **Upwind Difference Scheme (UDS):** this scheme is a first order scheme that takes in consideration the direction of the flow. It assigns the value of ϕ of the grid point that is on the *upwind* side of the face, so:

$$\begin{aligned} \phi_e &= \phi_P && \text{if } m_e > 0 \\ \phi_e &= \phi_E && \text{if } m_e < 0 \end{aligned} \quad (2.14)$$

- **Central Difference Scheme (CDS):** this is a second-order scheme that uses the arithmetic mean to calculate the variable at the face.

$$\phi_e = \frac{\phi_P + \phi_E}{2} \quad (2.15)$$

Introducing numerical schemes to the discretized equations, an algebraic equation that depends on the values of the neighbouring is obtained for each node. The structure of these equations is the following

$$a_P \phi_P = a_E \phi_E + a_W \phi_W + a_N \phi_N + a_S \phi_S + b_p \quad (2.16)$$

Where ϕ_i are the values of the variable at each neighbour node and a_i are the coefficients that affect these variables. b_p is a term that includes all the things that not depend on the value of the neighbour nodes, such as source terms.

A system of algebraic equations like this one is the system that has to be solved to obtain the distribution of ϕ along the whole domain.

2.2.2.2 Temporal discretization

In the previous point, the discretization of the transient term was left. The way in how this term is evaluated is very important for the calculation of a variable that changes in time and the structure of the CFD code.

In this study, two different methods are used for the time discretization:

- **Explicit methods:** the value of the new time-step is calculated using only the value of the previous step. Explicit methods require less computational time for each step but are not unconditionally stable. The value of the time-step needs to be below a maximum that has to be evaluated and is related with the mesh size. Both convective and diffusive terms have they own minimum time-step that ensure numerical stability and are constrained by the following expression, which is known as CFL condition [9]

$$\Delta t_C \leq 0.3 \left(\frac{\Delta x_i}{|u_i|} \right)_{max} \quad \Delta t_D \leq 0.2 \left(\frac{(\Delta x_i)^2}{\mu} \right)_{max} \quad (2.17)$$

Where Δt_C and Δt_D are the maximum values for the time-step, Δx_i is the characteristic size of each the control volume, $|u_i|$ is the modulus of the velocity of each control volume and μ is the dynamic viscosity. The maximum value of the global time-step has to be lower than the minimum of Δt_C and Δt_D .

- **Implicit methods:** with this method, the value of the time-step that is calculated depends on the previous values as well as the value of the new time-step. The great advantage of these methods is that they are unconditionally stable for any time-step. However, each time-step requires solving a non-trivial system of equations and the use of a solver, which increases significantly the computational power required. This high stability and the possibility to use larger time-steps make them optimal for steady cases. [8]

The two methods used in this study use a first-order approximation in time and the transient term integrated along a rectangular finite volume takes the form

$$\int_{\Omega} \rho \frac{\partial \phi}{\partial t} = \rho \frac{\phi^{n+1} - \phi^n}{\Delta t} \Delta x \Delta y \quad (2.18)$$

Introducing equation 2.18 into equation 2.12, the fully discretized equation for an explicit scheme is:

$$\begin{aligned} \rho \frac{\phi^{n+1} - \phi^n}{\Delta t} \Delta x \Delta y + [(\rho u \phi^n)_e - (\rho u \phi^n)_w] \Delta y + [(\rho v \phi^n)_n - (\rho v \phi^n)_s] \Delta x = \\ = \left[\left(\Gamma \frac{\partial \phi}{\partial x} \right)_e^n - \left(\Gamma \frac{\partial \phi}{\partial x} \right)_w^n \right] \Delta y + \left[\left(\Gamma \frac{\partial \phi}{\partial y} \right)_n^n - \left(\Gamma \frac{\partial \phi}{\partial y} \right)_s^n \right] \Delta y + S^n \Delta x \Delta y \end{aligned} \quad (2.19)$$

And for an implicit scheme:

$$\begin{aligned} \rho \frac{\phi^{n+1} - \phi^n}{\Delta t} \Delta x \Delta y + [(\rho u \phi^{n+1})_e - (\rho u \phi^{n+1})_w] \Delta y + [(\rho v \phi^{n+1})_n - (\rho v \phi^{n+1})_s] \Delta x = \\ = \left[\left(\Gamma \frac{\partial \phi}{\partial x} \right)_e^{n+1} - \left(\Gamma \frac{\partial \phi}{\partial x} \right)_w^{n+1} \right] \Delta y + \left[\left(\Gamma \frac{\partial \phi}{\partial y} \right)_n^{n+1} - \left(\Gamma \frac{\partial \phi}{\partial y} \right)_s^{n+1} \right] \Delta y + S^{n+1} \Delta x \Delta y \end{aligned} \quad (2.20)$$

Where the superscript n refers to the previous time-step and the superscript $n + 1$ to the new time-step.

2.2.3 Fractional step method

As it has been explained in previous pages, one of the main difficulties concerning the resolution of the Navier-Stokes equations is the strong coupling that exists between them. Different methods and strategies have been proposed along years to overcome this difficulty. In this study, a fractional step method will be used.

Alexandre J. Chorin and Roger Temam first introduced this method, which is also known as projection method, in the late 60's and it relies on the application of the Helmholtz-Hodge decomposition theorem to the Navier-Stokes equations.

Applying the theorem it can be demonstrated that the equation 2.5 in its dimensionless form can be spitted into a divergence-free vector and the gradient of a scalar field. The theorem assures that this decomposition is unique and the mathematical deduction leads to a Poisson equation for pressure. [10]

Then, the main idea is that in first place the velocity field \mathbf{u} is time-advanced without regard of the incompressible constraint imposed by equation 2.2 that will be later recovered by solving the pressure equation. This time-advanced velocity field is represented by the predictor velocity \mathbf{u}^p , that is uniquely decomposed into a divergence-free vector and the gradient of a scalar field

$$\mathbf{u}^p = \mathbf{u}^{n+1} + \nabla \tilde{p} \quad (2.21)$$

Where \mathbf{u}^{n+1} is the velocity in the following time-step, which fulfils the incompressibility constrain, and $\nabla \tilde{p}$ is the pseudo-pressure gradient. The predictor velocity distribution \mathbf{u}^p can be obtained from the previous velocity field \mathbf{u}^n using an

appropriate numerical scheme, depending on the case that is going to be studied. Once it is calculated, applying the divergence operator to equation 2.21 one can obtain

$$\nabla \cdot \mathbf{u}^p = \nabla \cdot \mathbf{u}^{n+1} + \nabla \cdot (\nabla \tilde{p}) \rightarrow \nabla \cdot \mathbf{u}^{n+1} = 0 \quad (2.22)$$

$$\Delta \tilde{p} = \nabla \cdot \mathbf{u}^p \quad (2.23)$$

This is the Poisson equation for pressure that must be solved using a specific solver to do so. With the pressure distribution obtained, then the solution for the next step velocity is straightforward

$$\mathbf{u}^{n+1} = \mathbf{u}^p - \nabla \tilde{p} \quad (2.24)$$

Overall this is the methodology that will be followed to solve the coupling in the Navier-Stokes equations. More detailed information about the discretized equations and numerical schemes used is found in the description of each particular case.

2.2.4 Mesh

As explained in section 2.2.1, the finite volume method relays on calculate the different variables on discrete points in the domain. So one of the first things that have to be done to do a numerical simulation is to discretize the domain and create what is known as a mesh.

2.2.4.1 Structured and unstructured meshes

There are different ways to obtain the discretized domain so there are also different types of meshes in function of the geometric shapes used or its distribution. The two basic types of mesh are:

- **Structured meshes:** in a structured mesh, the different control volumes are arranged following a determined pattern so every point has the same neighbours and they are ordered in a concrete way. The elements are quadrilateral in 2D and hexahedral in 3D. A structured mesh can also be uniform, if all the elements have the same size, or non-uniform, if different sizes are used. Working with this type of mesh is easier and require less memory. [11]
- **Unstructured meshes:** in this type of mesh the distribution of control volumes did not follow any order. The elements are usually triangles in 2D and tetrahedral in 3D.

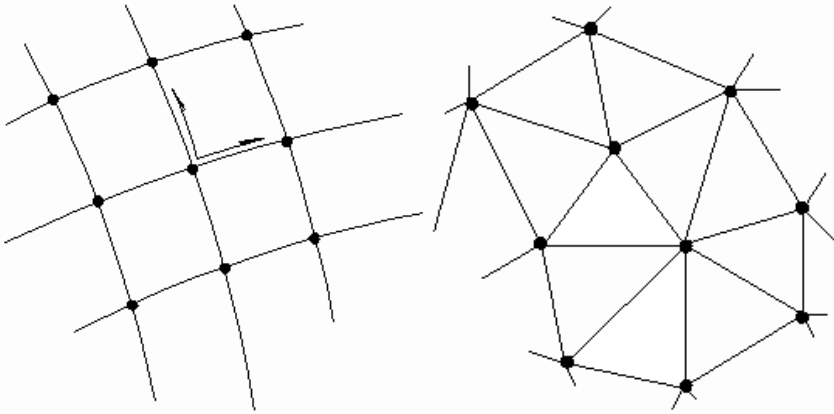


Figure 2.2: Examples of structured (left) and unstructured mesh (right). Extracted from: [11]

On one hand, structured meshes offer an advantage on computational performance, as they do not need to store the connectivity (neighbouring relations) for each node and the solver can take advantage of its constant and ordered distribution. Historically there are a lot of different solvers developed for structured meshes, as they are usually more efficient and easier to be programmed. Another advantage of structured meshes is that they also offer a better resolution.

On the other hand, unstructured meshes have to deal with a complex nodal connectivity, which means more computational power required, but are a powerful tool to discretize domains with complex geometries.

The quality and the resolution of the mesh are closely related with its number of elements. As many elements, more resolution can be obtained. However, the fact of having more elements also means that more calculations have to be done so the computer power required is superior.

In order to save computational time in problems where the variables studied have a very different behaviour along the domain, control volumes can be concentrated on the regions that have more interest or the flow has a more complex behaviour, like in the boundaries or near an object. This strategy reduces the number of nodes needed as well as the computer load but without losing resolution in the more interesting areas. The following picture shows the difference between a uniform and a non-uniform structured grid.

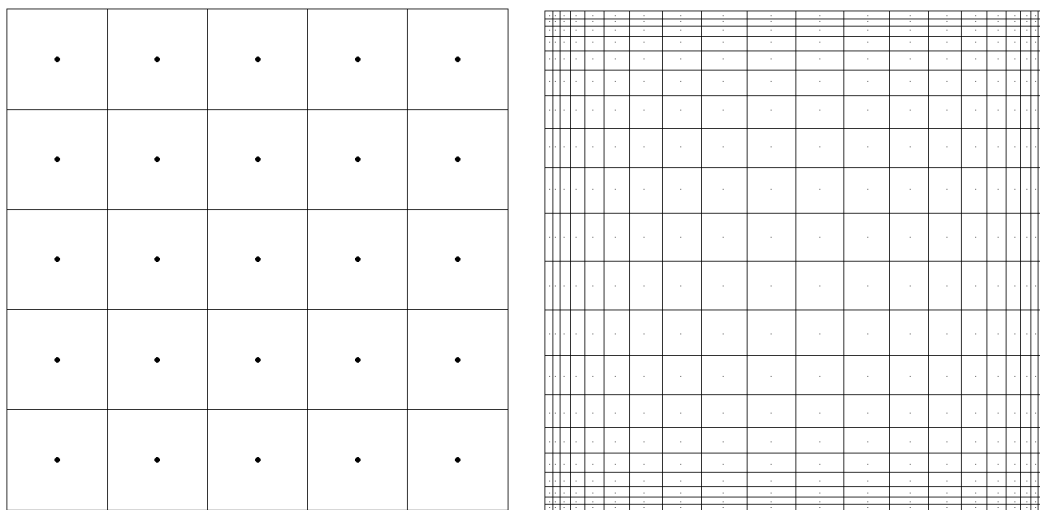


Figure 2.3: Structured uniform mesh (left) and structured non-uniform mesh (right)

These two kinds of meshes showed in Figure 2.3 are the ones that will be used to perform the simulations in this study.

2.2.4.2 Collocated and staggered meshes

When structured meshes are used, there is another important thing that has to be taken into account regarding the discretization of the domain. The problem is known as the *checkerboard* problem [12] or *odd-even decoupling* and it is related with the way in which the velocity components are calculated.

Remember from equation 2.24 that the velocity depends on the pressure gradient but not on the pressure itself. If all the variables are calculated in the same grid points, when the velocity correction is applied it can be found that in a particular node the value of the velocity depends on the values of the pressure in the adjacent nodes but not in the pressure value of the node itself. This means that a pressure field with alternate values between adjacent nodes can fulfil the equations constrains but, as it is imaginable, it cannot represent a real physical phenomenon.

To overcome this problem that appear in structured *collocated* meshes (meshes where all the variables are calculate in the same points), the solution used in this study is to use *staggered* meshes. In this kind of meshes, the velocity components are calculated on the faces of the control volumes of the “main” grid, where the rest of the variables are obtained. In Figure 2.4 there is an example of a staggered mesh used in this study. In black there are the main nodes and control volumes, in red the *x-staggered* nodes, where the horizontal component of the velocity is calculated, and in green the *y-staggered* nodes, in which the vertical component is obtained.

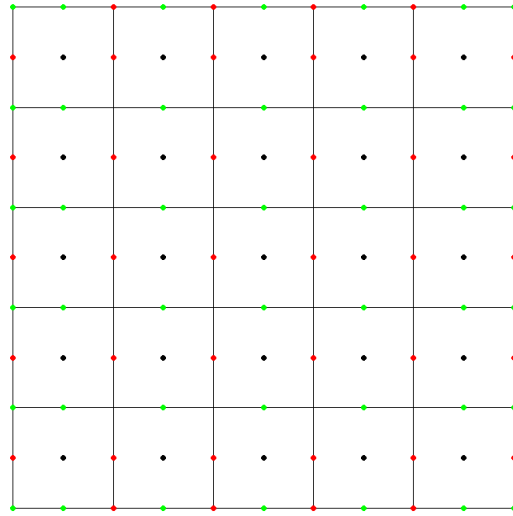


Figure 2.4: Staggered mesh used to calculate the different components of the velocity

2.2.5 Solvers

A solver is software used to obtain the solution of non-trivial mathematical problems that usually require doing a huge amount of calculations, like the system of linear equations that is obtained after the discretization of the Navier-Stokes equations or the Poisson equation for pressure.

The cases involved in these study lead to the resolution of a system of linear equations with the form of equation 2.16 that can be written in matrix form as

$$A \cdot x = b \quad (2.25)$$

Where A is a matrix of $n \times n$ dimensions formed by the a_i coefficients, x is a row vector with n components that represent the solution of the system and b is a similar vector with the same n components formed by the b_i coefficients. n is the number of discrete points of the mesh.

There are different types of solvers that can work with a system like this one. In a first approach, they can be split in two main types:

- **Iterative solvers:** this kind of solvers uses an initial guess to generate successive approximations to the solution. After each iteration, the new values calculated are compared with the last ones until the error between them is smaller than previous defined *convergence criteria*. The precision of the final solution depends on how strict is this criteria.
- **Direct solvers:** this methods attempt to deliver an exact solution of the system using a finite sequence of operations and mathematical techniques.

Direct solvers are usually much faster than iterative solvers as the solution is achieved calculating all the variables only once. Nevertheless, they are more difficult to implement and their implementation also depends on the typology of the system that has to be solved. In the following points, there is a brief description of the methods used for the resolution of systems of linear equations in this study.

2.2.5.1 Gauss-Seidel

The German mathematicians Carl Friedrich Gauss and Philipp Ludwig von Seidel proposed this method, which is also known as the Liebmamn method or the method of successive displacement, in the 19th century. It is an iterative method whose convergence is only guaranteed if the A matrix is either diagonally dominant or symmetric and positive definite. [13]

From equation 2.16 the following expression can be obtained of each node

$$\phi_P^{n+1} = \frac{a_E \phi_E^n + a_W \phi_W^n + a_N \phi_N^n + a_S \phi_S^n + b_p}{a_p} \quad (2.26)$$

Notice that ϕ stands for the solution of the system expressed by x in equation 2.25. ϕ^{n+1} is the value calculated in the present iteration while ϕ^n is the last value calculated.

Once ϕ_P^{n+1} is calculated for all the nodes in the domain, then the convergence criteria needs to be evaluated

$$a_p \phi_P^{n+1} - (a_E \phi_E^{n+1} + a_W \phi_W^{n+1} + a_N \phi_N^{n+1} + a_S \phi_S^{n+1} + b_p) < \varepsilon \quad (2.27)$$

Where ε is the residual or convergence criteria. If the condition expressed in 2.27 is reached, the solution is obtained. In a transient problem this condition has to be fulfilled for every time-step.

2.2.5.2 TDMA

TDMA stands for *Tri-diagonal matrix algorithm* and it is a direct method to solve tri-diagonal systems of equations, which are the systems whose A matrix is characterised to have nonzero elements only on the main diagonal and on the first diagonal below and above the main one. This kind of matrix is common in 1D problems related with the resolution of a Poisson equation. [14] The discretized equations have a form like

$$a_p \phi_P = a_E \phi_E + a_W \phi_W + b_p \quad (2.28)$$

TDMA method is a kind of LU decomposition, where the system matrix is decomposed into two triangular matrix, one with zeros in the upper part of the diagonal and the other with zeros in the lower part of the diagonal.

$$Ax = b \rightarrow LUx = b \quad (2.29)$$

$$\text{if } Ux = z \rightarrow Lz = b \quad (2.30)$$

As we are dealing with a system of only 3 diagonals, the matrixes U and L will only have 2 diagonals. It can be supposed that the matrix U and z will have a structure like

$$U = \begin{pmatrix} 1 & -P(1) & 0 & \dots \\ 0 & 1 & -P(2) & \ddots \\ 0 & 0 & 1 & \ddots \\ \vdots & \ddots & \ddots & \ddots \end{pmatrix} z = \begin{pmatrix} R(1) \\ R(2) \\ R(3) \end{pmatrix} \quad (2.31)$$

Where $P(i)$ and $R(i)$ are function of the discretization coefficients a_i and b_i . Then the solution will be

$$\phi_P = P_P \phi_E + R_P \quad (2.32)$$

$$\phi_W = P_W \phi_P + R_W \quad (2.33)$$

Substituting this on equation 2.28 one can obtain:

$$a_P \phi_P = a_E \phi_E + a_W [P_W \phi_P + R_W] + b_p \quad (2.34)$$

Re-ordering terms:

$$[a_P - a_W P_W] \phi_P = a_E \phi_E + a_W R_W + b_p \quad (2.35)$$

And finally identifying terms to match a structure like equation 2.31 it results:

$$P_P = \frac{a_E}{a_P - a_W P_W} \quad R_P = \frac{a_W R_W + b_p}{a_P - a_W P_W} \quad (2.36)$$

It can be seen from equation 2.32 that the values of ϕ_P will only depend on the value of the variable ϕ_E situated in the East side. Starting on the node situated at the East end of the domain, all the other values can be obtained going across the domain from East to West.

2.2.5.3 Line-by-line method

As explained before, direct solvers like TDMA are much faster than iterative methods like Gauss-Seidel. However, the problems that are going to be solved in this study are two-dimensional and the system of equations obtained has not a tri-diagonal matrix but a penta-diagonal matrix. This fact is easy to understand; as we are adding two neighbours in each node, the value at that point will depend on two more coefficients resulting in a matrix with five diagonals with nonzero values instead of the three found in one-dimensional problems.

The approach followed in this study is to use a combination of the two methods that have been explained before. Starting with a guess value, a TDMA algorithm swipes all the rows of the 2D domain obtaining an approximate solution. This solution is used as

a guess for another TDMA algorithm that swipes again the domain but this time following all the columns. After this, the values obtained by the second swipe of the TDMA algorithm are compared with the first guess values until convergence is reached, like in a Gauss-Seidel method.

What the method is really doing is transforming the penta-diagonal matrix of the system in series of tri-diagonal matrixes that are solved using a TDMA and comparing the results obtained for the previous swipe of the TDMA algorithm with the new ones.

To do so, equation 2.16 with five a_i values is transformed into an equation that has only three a_i values with the following approximation when swiping the different rows

$$a_P \phi_P = a_E \phi_E + a_W \phi_W + b_p^* \quad (2.37)$$

$$b_p^* = b_p + a_N \phi_N + a_S \phi_S \quad (2.38)$$

And this one when swiping the domain for each column:

$$a_P \phi_P = a_N \phi_N + a_S \phi_S + b_p^* \quad (2.39)$$

$$b_p^* = b_p + a_E \phi_E + a_W \phi_W \quad (2.40)$$

The line-by-line method is not a direct solver but the fact of swiping all the rows and columns and obtaining all the values at once, improves significantly its performance in comparison with only using a Gauss-Seidel algorithm.

3 Code verification

Before doing any simulation using the finite volume code developed has to pass through a testing and verification process to ensure that there are no errors and the solutions obtained keep to reality. In other words, to know that the program is doing what is expected to do.

Even for a very simple case, the code can easily have hundreds of lines and several functions, each one designed for a specific task: the mesh generation, the solver, the numerical scheme or all the discretized equations. All these functions have to join with each other and be able to share the information in a proper way.

The following sections are focused on determine the correct operation of the numerical code developed, using different techniques and comparing the results obtained with analytical results or benchmark cases.

3.1 Method of manufactured solutions

This method described by Roache relies on the comparison between the solutions obtained by the CFD software and the solution of an arbitrary analytic function.

As explained in previous sections, the numerical code uses different discrete mathematical operators to solve the Navier-Stokes equations. In fact, these discretized operators have to do the same as the continuous mathematical operators they derive from.

The MMS consist on taking an arbitrary analytic function \mathbf{u}_a that is a solution of the PDE system and the source term \mathbf{f}_a associated with it, which is calculated analytically. Then, the source term is evaluated at the discretization nodes and used as input for the numerical code. The numerical solution obtained \mathbf{u}_n is then compared to the analytical one, swiping the entire domain [15]

$$\|\mathbf{e}\|_\infty = \|\mathbf{u}_a - \mathbf{u}_n\|_\infty \quad (3.1)$$

The solution is tested for several mesh sizes and the error must tend to zero when the grid is refined with the expected order of accuracy of the numerical scheme.

Using the MMS also brings the possibility to test separately different parts and discrete operators. For example, the convective term is a function implemented in the code that calculates the divergence of a vector field or the diffusive term that in fact is a discrete Laplace operator.

3.1.1 Diffusive term

Evaluating if the diffusive term is doing what it has to do is quite easy. Equation (2.5) shows that this term calculates the laplacian of the velocity field multiplied by the kinematic viscosity of the fluid. It is known that this operator is equivalent the sum of all the unmixed second partial derivatives in Cartesian coordinates.

If the input of the function *diffusive* is changed and instead of the velocity field an analytic function whose second derivative is known is given, the numerical code would give an approximation of this second derivative. There are a lot of functions that can be used but the following ones have been used

$$\mathbf{f}_a = \cos(x) \cdot \sin(y) \quad (3.2)$$

$$\mathbf{u}_a = \Delta \mathbf{f}_a = -2 \cos(x) \cdot \sin(y) \quad (3.3)$$

Equation 3.2 is evaluated in all the grid points and then the numerical scheme calculates the laplacian. The process is repeated for different mesh sizes and the following plot is obtained.

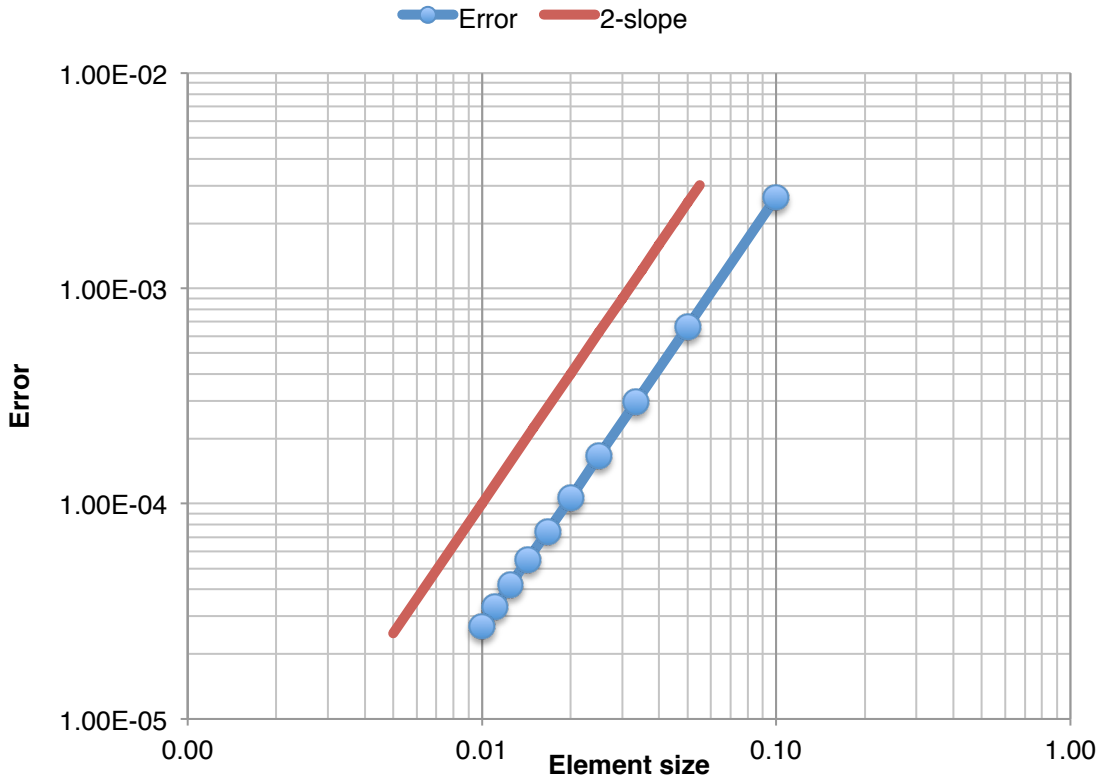


Figure 3.1: Error norm versus element size for the diffusive term

A second-order CDS scheme has been used to evaluate the functions and it can be seen that the norm of the error tends to 0 with the expected rate of decreasing.

3.1.2 Convective term

Equation 2.9 shows that the convective term is calculating the divergence of a vector field so in this case the input to the *convective* function will be a vector field whose divergence is known. The best option is to use a conservative vector field because its divergence is 0.

The flow used in the test is known as Taylor-Green vortex and is represented by:

$$u = \cos(x) \cdot \sin(y) \quad (3.4)$$

$$v = -\cos(x) \cdot \sin(y) \quad (3.5)$$

Its divergence is 0, $\nabla \cdot \mathbf{u} = 0$, so the result given by the numerical scheme should tend to this value as the grid used is more refined.

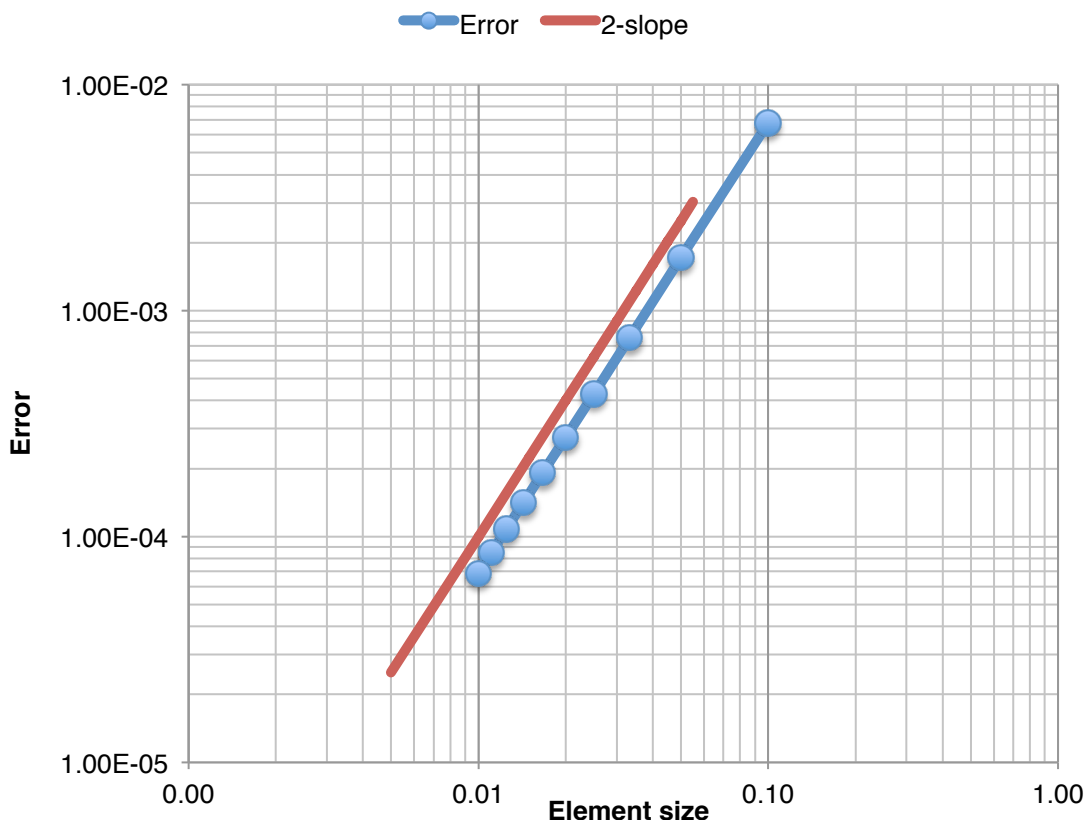


Figure 3.2: Error norm versus element size for the convective term

It can be seen that, using also a second-order CDS scheme, the behaviour of the norm of the error matches perfectly the 2-slope line.

3.2 Smith-Hutton problem

The Smith-Hutton problem is a previous step to the resolution of the full set of Navier-Stokes equations. This case concerns about the resolution of a *convection-diffusion* equation like 2.9 in a 2D domain without any source term and a prescribed velocity field. The results obtained are compared with the ones presented at [16].

3.2.1 Governing equations and boundary conditions

As explained in the description, in this problem the equation that has to be solved is the following:

$$\frac{\partial \rho\phi}{\partial t} + \nabla(\rho\mathbf{u}\phi) = \nabla(\Gamma\nabla\phi) \quad (3.6)$$

The solution that has to be achieved is the distribution of ϕ along the whole domain. Additionally, velocity field is prescribed so there is no need to be concerned about the velocity-pressure coupling, because in this case it does not exist. There is no need to use a specific approach like the FSM to obtain the velocity field in each time-step because it is constant and given by

$$u(x, y) = 2y(1 - x^2) \quad (3.7)$$

$$v(x, y) = -2x(1 - y^2) \quad (3.8)$$

Variable ϕ has also a boundary conditions defined

$$\phi = 1 + \tanh(\alpha(2x + 1)) \quad \text{at } y = 0; x \in (-1, 0) \text{ (inlet)} \quad (3.9)$$

$$\frac{\partial \phi}{\partial y} = 0 \quad \text{at } y = 0; x \in (0, 1) \text{ (outlet)} \quad (3.10)$$

$$\phi = 1 - \tanh(\alpha) \quad (\text{elsewhere}) \quad (3.11)$$

Where $\alpha = 10$. These are all constrains and equations needed to solve the Smith-Hutton problem. In Figure 3.3 there is a graphical representation of the domain.

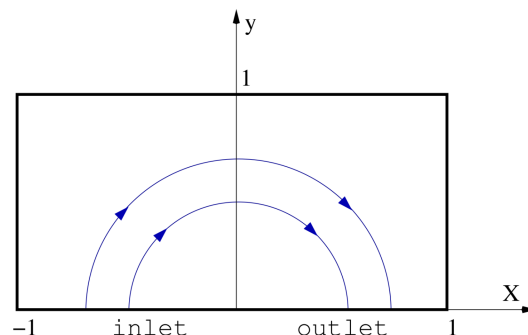


Figure 3.3: Representation of the domain and the flow for the Smith-Hutton problem

As it can be seen there is a rectangular domain defined from $x \in [-1,1]$ and $y \in [0,1]$. The solution is obtained for different relations of $\rho/\Gamma = 10, 10^3$ and 10^6 , which represent a balance between the importance of convection or diffusion in the transport of physical quantities.

3.2.2 Numerical method

In this problem, the equation that is simulated is directly equation 2.20 without the source term

$$\begin{aligned} \rho \frac{\phi^{n+1} - \phi^n}{\Delta t} \Delta x \Delta y + [(\rho u \phi^{n+1})_e - (\rho u \phi^{n+1})_w] \Delta y + [(\rho v \phi^{n+1})_n - (\rho v \phi^{n+1})_s] \Delta x = \\ \left[\left(\Gamma \frac{\phi_E - \phi_P}{d_{EP}} \right)^{n+1} - \left(\Gamma \frac{\phi_P - \phi_W}{d_{PW}} \right)^{n+1} \right] \Delta y + \left[\left(\Gamma \frac{\phi_N - \phi_P}{d_{NP}} \right)^{n+1} - \left(\Gamma \frac{\phi_P - \phi_S}{d_{PS}} \right)^{n+1} \right] \Delta x \end{aligned} \quad (3.12)$$

Notice that an implicit time-discretization is used, so there is no limitation in time-step that can be used.

The evaluation of the variables at the faces of the control volume is done by a first-order UDS and with a second-order CDS. The CDS scheme is only used for the case of $\rho/\Gamma = 10$ because it does not work properly in cases where there is very low diffusion and a direct solver is used [12].

3.2.3 Results

The solution has been analysed for different relations of the *advection-diffusion* coefficient ρ/Γ and different mesh sizes: 100x50 elements, 200x100 elements and 400x200 elements.

x-position	$\rho/\Gamma = 10$		$\rho/\Gamma = 10^3$		$\rho/\Gamma = 10^6$	
	Benchmark	400x200 UDS	Benchmark	400x200 UDS	Benchmark	400x200 UDS
0	1,989	1,9885	2	2	2	2
0,1	1,402	1,4011	1,999	2	2	2
0,2	1,146	1,1456	1,999	1,9991	2	1,9999
0,3	0,946	0,9463	1,985	1,9737	1,999	1,9959
0,4	0,775	0,7752	1,841	1,7166	1,964	1,8514
0,5	0,621	0,6218	0,951	0,9426	1	0,9588
0,6	0,480	0,4813	0,154	0,2309	0,036	0,1359
0,7	0,349	0,3511	0,001	0,0215	0,001	0,0052
0,8	0,227	0,2294	0,000	0,0008	0,000	0,0001
0,9	0,111	0,1142	0,000	0	0,000	0
1	0,000	0	0,000	0	0,000	0

Table 3.1: Results comparison of the solution obtained using a 400x200 element mesh

In the previous Table 3.1 there are the results obtained at the outlet using the finest mesh along with the results of the benchmark solution. It can be seen that the results using this mesh are quite accurate and in general the differences between the numerical solution obtained with the self-developed code and the one proposed are small.

However, the differences obtained suffer a significant increase for the higher values of ρ/Γ in the central part of the outlet. This is a consequence of using UDS numerical scheme because this kind of scheme suffers from what is known as *false diffusion*. It can be demonstrated that the error included by the first-order approximation can be seen as a contribution to the diffusive term that is more pronounced when the diffusion coefficient has a very low value. For more information about the *false or numerical diffusion* refer to [12].

This phenomenon can be seen graphically in Figure 3.4 and Figure 3.5, where there is the distribution of ϕ at the outlet for different mesh sizes. The plots show the difficulties that the numerical scheme has when there is an abrupt change of the variable. With denser meshes, the phenomenon is soften but it is impossible to avoid completely the numerical diffusion.

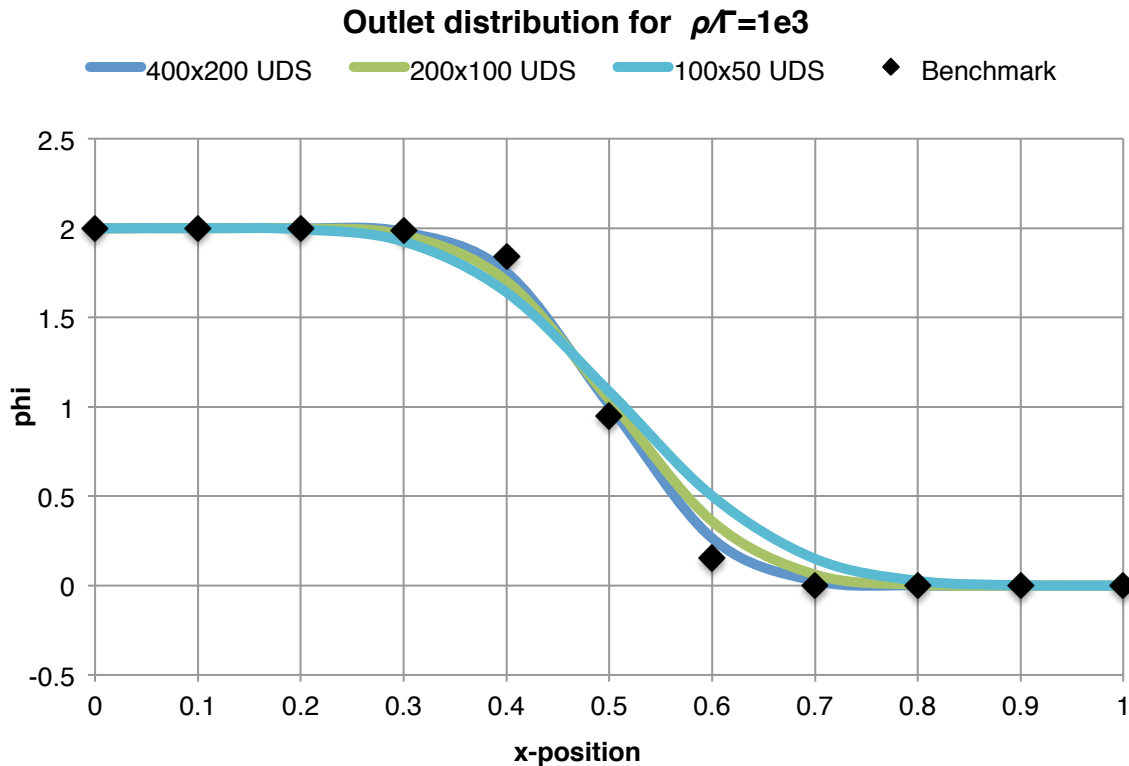


Figure 3.4: Outlet distribution for $\rho/\Gamma = 1e3$ with different mesh sizes

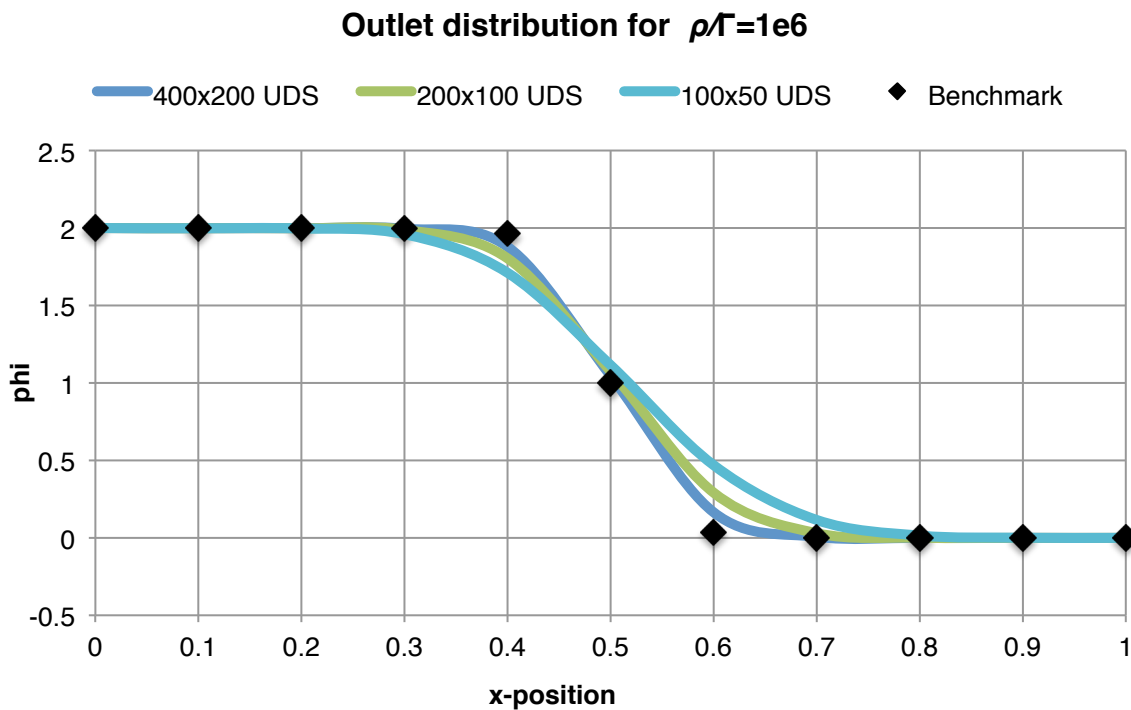


Figure 3.5: Outlet distribution for $\rho/\Gamma = 1e6$ with different mesh sizes

Another verification that can be done is to check if the error is following the expected tendency as the mesh used is finer. In the cases where a UDS scheme is used to approximate the convective term, the norm of the error should follow a line of slope 1 as well as the tendency when using a CDS scheme should be a 2-slope line

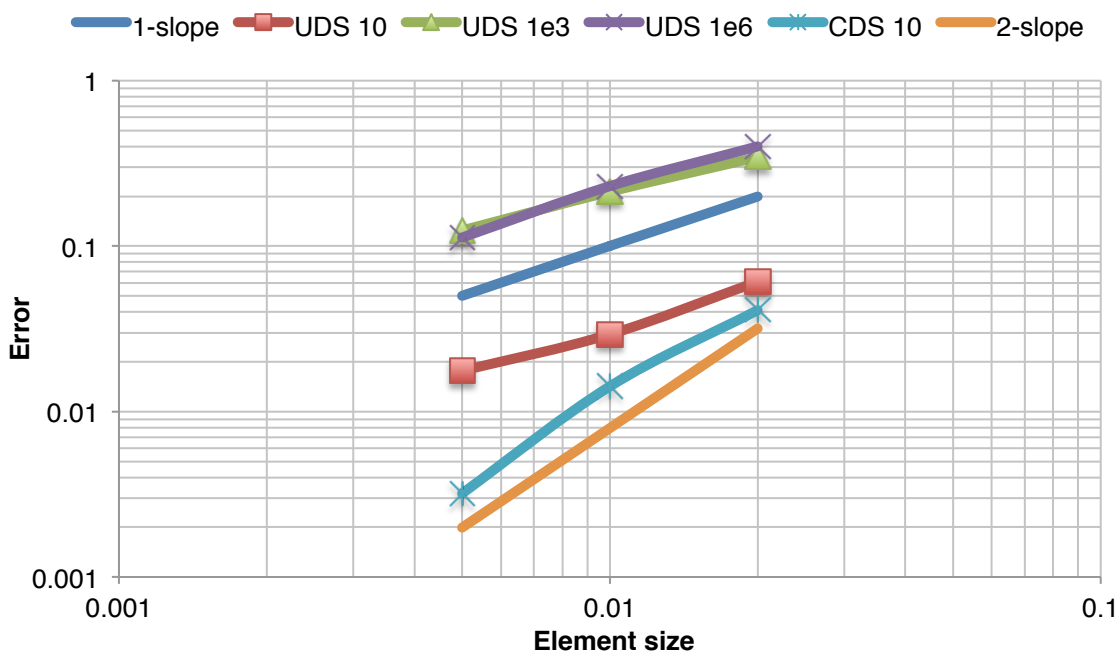


Figure 3.6: Error norm versus element size for different cases and numerical schemes

The plot in Figure 3.6 shows the expected behaviour for all cases. So the conclusion that can be extracted is that the software is doing what is expected in the resolution of a convection-diffusion equation, with the singularities of the numerical solution.

3.3 Driven cavity problem

The driven cavity problem consists of a 2D square cavity with no-slip conditions at the lateral and bottom walls and a forced velocity flow at the top surface. There is no heat transfer through the wall surfaces. In this problem, incompressible Navier-Stokes equations (momentum and continuity) are solved using direct numerical simulation. The flow is simulated in different Re regimes and the solution obtained is compared to benchmark results [17].

3.3.1 Governing equations and parameters

Let's take the non-dimensional form of continuity and momentum equations. All the hypothesis considered in 2.1 are also taken and body forces are neglected [10], [18]

$$\nabla \cdot \mathbf{u} = 0 \quad (3.13)$$

$$\frac{\partial \mathbf{u}}{\partial t} + (\mathbf{u} \cdot \nabla) \mathbf{u} = \frac{1}{Re} \Delta \mathbf{u} - \nabla p \quad (3.14)$$

Where $Re = \frac{\rho V_0 L}{\mu}$ is the Reynolds number, \mathbf{u} is the dimensionless velocity vector, t is the dimensionless time and p the dimensionless static pressure. ρ and μ are, respectively, the density and the dynamic viscosity of the fluid while V_0 and L are the characteristic velocity and length of the problem. These last values are dimensionless and defined in the proper way to match the Re number that will be simulated:

- Top wall horizontal velocity, $V_0 = 1$
- Length of the cavity, $L = 1$
- Density of the fluid, $\rho = 1$
- Dynamic viscosity is defined by the chosen Re , $\mu = \frac{1}{Re}$

3.3.2 Boundary conditions

For the velocity the boundary conditions are quite easy. The problem is defined with no-slip conditions at all walls unless the top wall where a horizontal velocity $u = V_0$ is imposed. As the simulation works with dimensionless variables, $V_0 = 1$ and the boundary conditions for velocity remain as

$$u = 1, v = 0 \quad \text{at } y = 1; x \in (0,1) \quad (3.15)$$

$$u = 0, v = 0 \quad \text{elsewhere} \quad (3.16)$$

For the pressure the restrictions are a little bit different. At the walls, as a boundary layer is created the boundary condition that fits better with this phenomenon is to set the gradient of pressure to 0 in the perpendicular direction towards the wall.

At the nodes where the velocity is prescribed, one can say that $\mathbf{u}^{n+1} = \mathbf{u}^p$ so for equation 2.24 it can be seen that the pressure gradient has to be also 0 in the direction of the velocity that is prescribed. So finally the boundary conditions for pressure are

$$\frac{\partial p}{\partial y} = 0 \quad \text{at } y = 0, y = 1; x \in (0,1) \quad (3.17)$$

$$\frac{\partial p}{\partial x} = 0 \quad \text{at } x = 0, x = 1; y \in (0,1) \quad (3.18)$$

And with all this conditions, the problem is closed and the solution can be evaluated.

3.3.3 Numerical method

The domain is discretised using the finite volume method using refined structured meshes with Cartesian coordinates. In refined meshes, volume controls are concentrated near the walls to obtain detailed information of the vortex that appear in these regions for higher values of Re number. To do so, a hyperbolic tangent function has been used to determine the position of the nodes

$$x = \frac{L}{2} \left(1 + \frac{\tanh \left(\gamma \left(\frac{2i}{Nx + 1} - 1 \right) \right)}{\tanh \gamma} \right) \quad (3.19)$$

Where x is the horizontal coordinate, L is the cavity length, γ is the concentration parameter set to $\gamma = 2$, Nx is the total number of horizontal volumes and i the position of the node. As it is a square cavity, the vertical coordinates are calculated in the same way.

To avoid unrealistic situations like the *checkerboard* problem [12], velocities are calculated in the faces of the control volumes using staggered meshes. There is one staggered mesh for each one of the velocity components. Pressure is calculated in the central nodes.

A second-order CDS scheme is used to evaluate the convective term and Fractional Step Method to solve the velocity-pressure coupling. Equation 3.14 can be rewritten as

$$\frac{\partial \mathbf{u}}{\partial t} = R(\mathbf{u}) - \nabla p \quad (3.20)$$

Where the term $R(\mathbf{u})$ represents the convective and diffusive terms:

$$R(\mathbf{u}) = -(\mathbf{u} \cdot \nabla) \mathbf{u} + \frac{1}{Re} \Delta \mathbf{u} \quad (3.21)$$

$R(\mathbf{u})$ is discretized in space following the methodology explained in 2.2.2.1 and with the second-order CDS scheme.

For the temporal discretization, a fully explicit second-order Adams-Bashforth scheme is used. The temporal discretized equations obtained are

$$\begin{aligned} \frac{\mathbf{u}^{n+1} - \mathbf{u}^n}{\Delta t} &= \frac{3}{2} R(\mathbf{u})^n - \frac{1}{2} R(\mathbf{u})^{n-1} - \nabla p^{n+1} \\ \nabla \cdot \mathbf{u}^{n+1} &= 0 \end{aligned} \quad (3.22)$$

Remember from 2.2.3 that the Fractional Step Method provides consists of calculating a time-advanced predictor velocity field

$$\mathbf{u}^p = \mathbf{u}^{n+1} + \nabla \tilde{p} \quad (3.24)$$

Taking \mathbf{u}^{n+1} from equation 3.22 and introducing it value to equation 3.24 the following equation can be obtained

$$\mathbf{u}^p = \mathbf{u}^n + \Delta t \left(\frac{3}{2} R(\mathbf{u})^n - \frac{1}{2} R(\mathbf{u})^{n-1} \right) \quad (3.25)$$

In this case the pseudo-pressure equals $\tilde{p} = \Delta t p^{n+1}$ and as expected the term is cancelled in equation 3.25. With the value of the predictor velocity, the Poisson equation for pressure can be solved

$$\Delta p^{n+1} = \frac{1}{\Delta t} (\nabla \cdot \mathbf{u}^p) \quad (3.26)$$

The resolution of equation 3.26 is not trivial. The equation is discretized and for each node a equation like 2.16 is obtained. The result is a system of linear equations that can be solved using an iterative solver, which in this case is a line-by-line method (Gauss-Seidel + TDMA). After this, the velocity for the next time-step is obtained easily

$$\mathbf{u}^{n+1} = \mathbf{u}^p - \Delta t \nabla p^{n+1} \quad (3.27)$$

The procedure is repeated for each time-step until convergence is reached with the defined precision. Notice that the procedure described involves an explicit time-discretization so the CFL condition, specified in section 2.2.2.2, has to be taken into account and the value of the time-step is determined to ensure numerical stability.

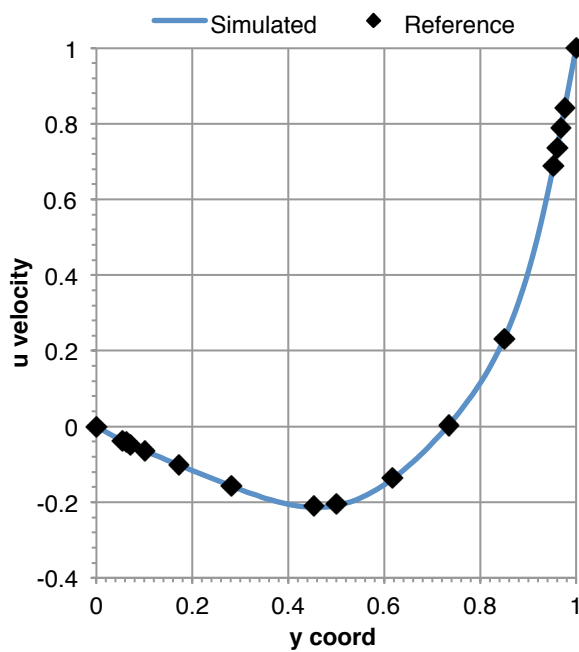
3.3.4 Results

The simulations have been carried out for different regimes for different values of Reynolds number: 100, 400, 1.000, 3.200, 5.000, 7.500 and 10.000. The results obtained using the self-developed code have been compared to the reference ones [17]. These results were obtained using numerical methods more than 30 years ago, but their reliability is very well considered.

The following plots show the evolution of the horizontal component of the velocity along the vertical centreline of the cavity and the vertical component of the velocity along the horizontal centreline. The simulated values and the reference ones are put together in the same graph to facilitate the comparison and evaluate the results.

The simulated results have been obtained using a refined mesh of 100x100 control volumes. The decision to use a refined mesh was taken to obtain a better representation of eddies that appear in the corners of the cavity, near the walls. For low Reynolds numbers, a coarser uniform mesh could be used to save computer power, as the nature of the flow is much more steady. However, the same refined mesh is used to all regimes to compare the performance of the code in the same conditions.

Centerline velocities at $Re = 100$



100 x 100 element mesh

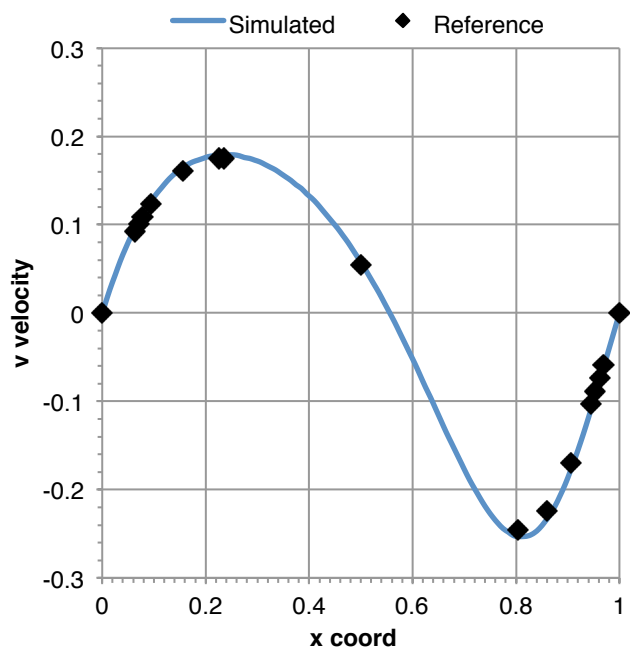
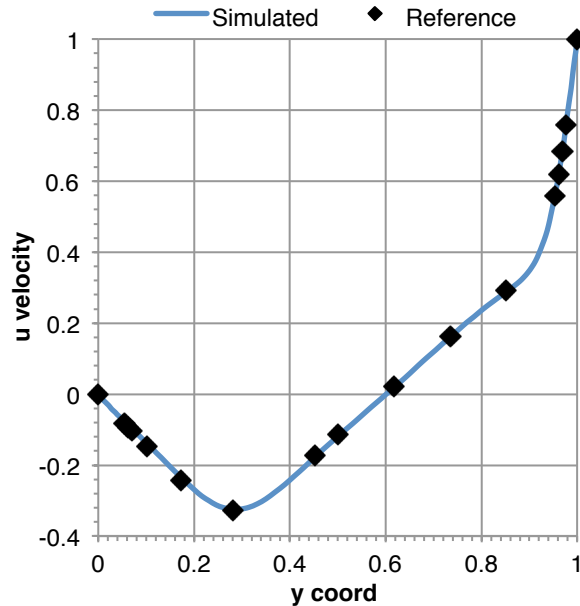


Figure 3.7: Centerline velocities comparison at $Re = 100$

Centerline velocities at $Re = 400$



100 x 100 element mesh

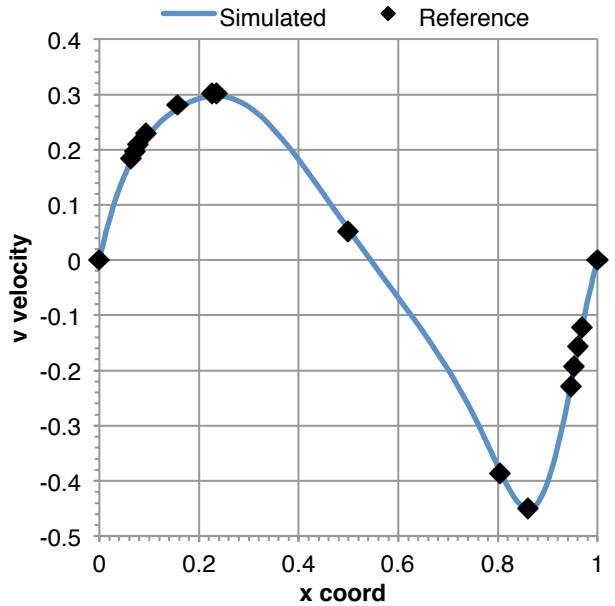
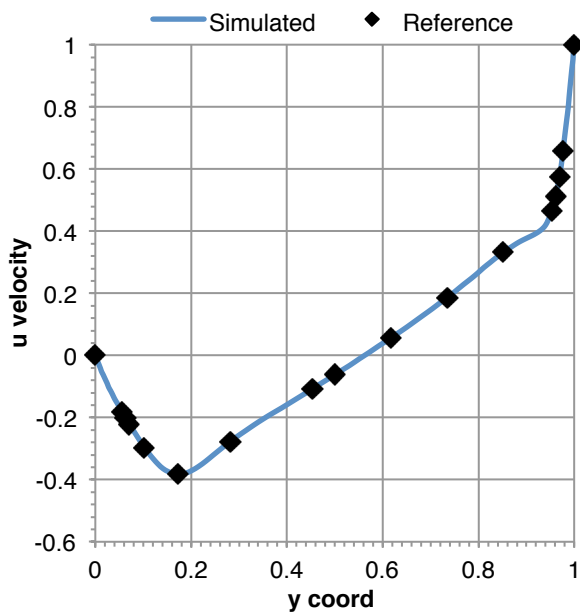
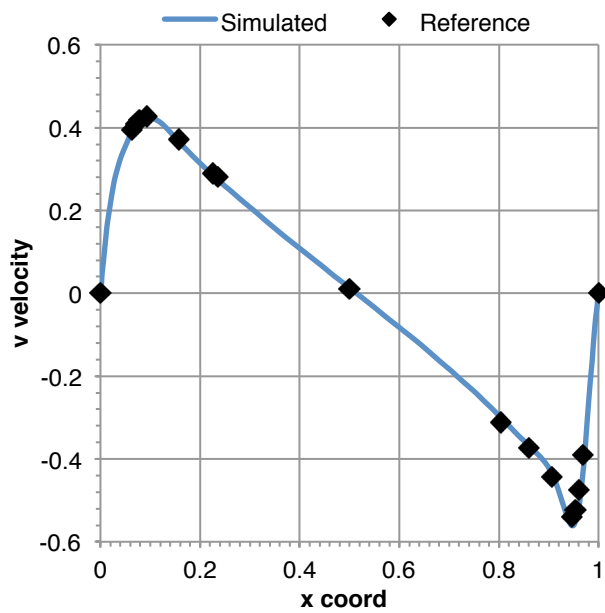
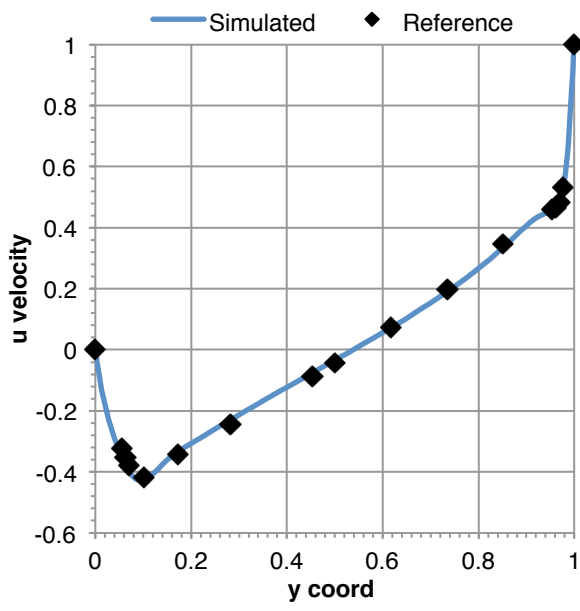
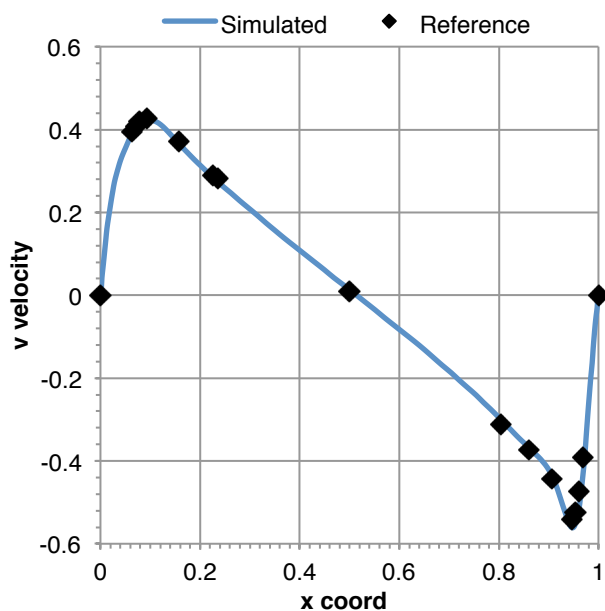


Figure 3.8: Centerline velocities comparison at $Re = 400$

Centerline velocities at $Re = 1000$ **100 x 100 element mesh****Figure 3.9:** Centerline velocities comparison at $Re = 1.000$ **Centerline velocities at $Re = 3200$** **100 x 100 element mesh****Figure 3.10:** Centerline velocities comparison at $Re = 3.200$

Centerline velocities at $Re = 5000$

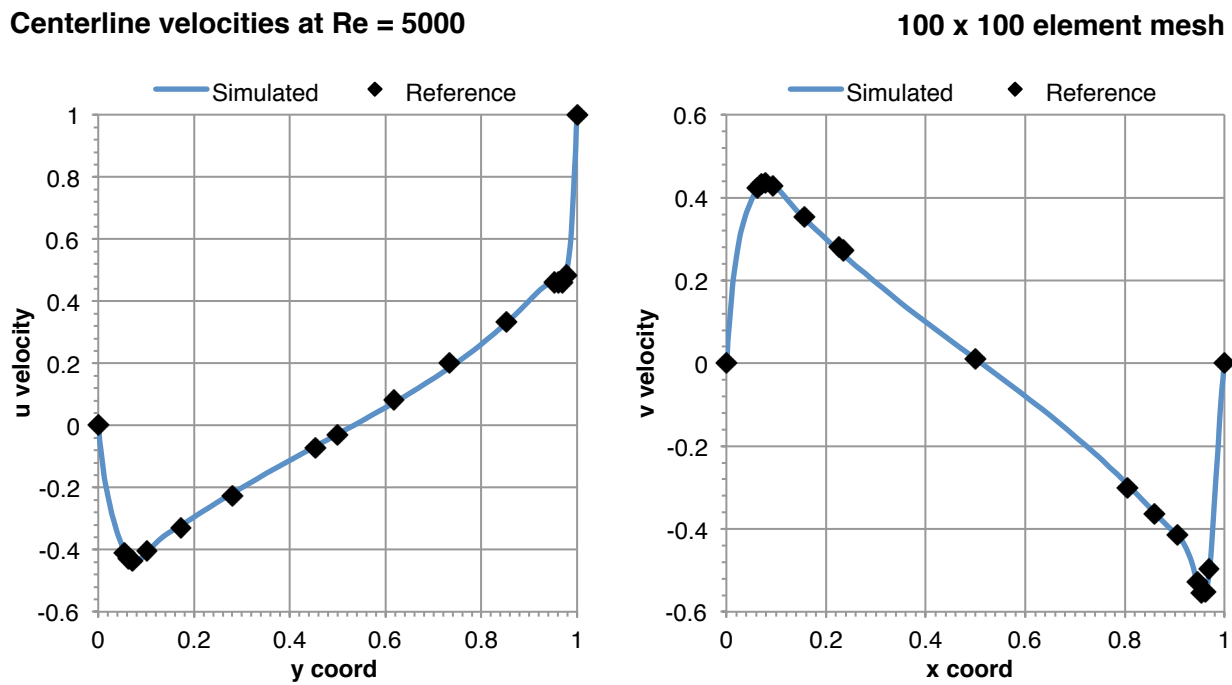


Figure 3.11: Centerline velocities comparison at $Re = 5.000$

Centerline velocities at $Re = 7500$

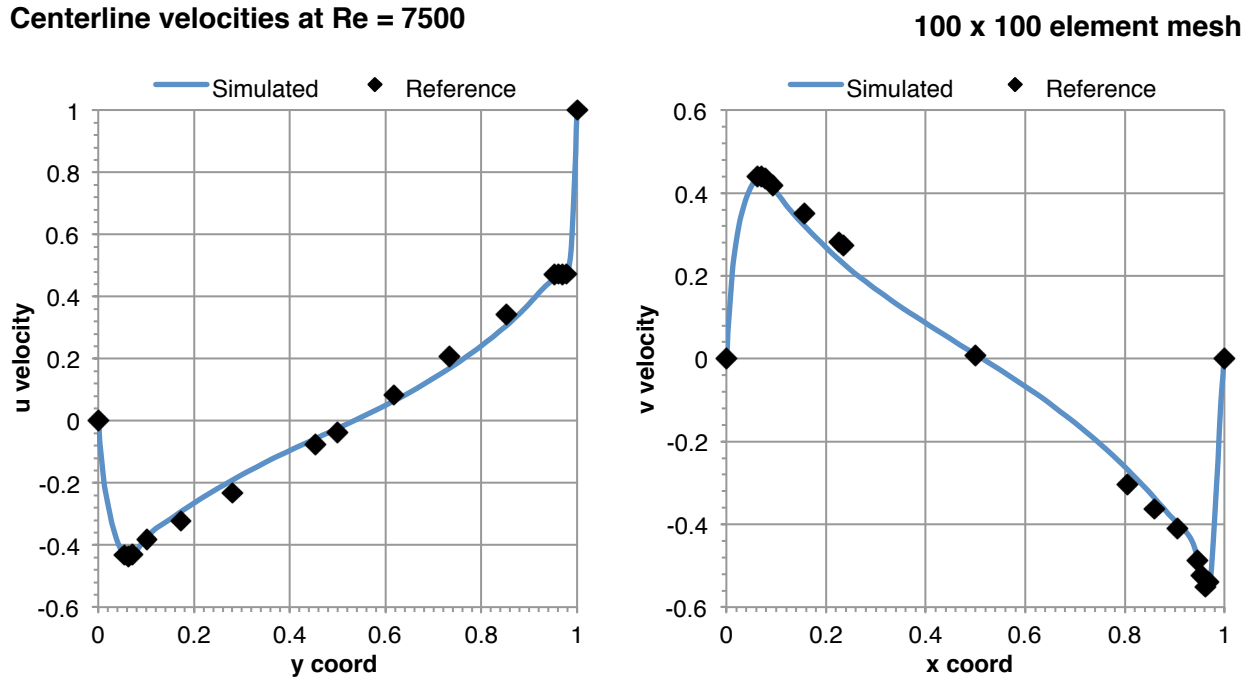
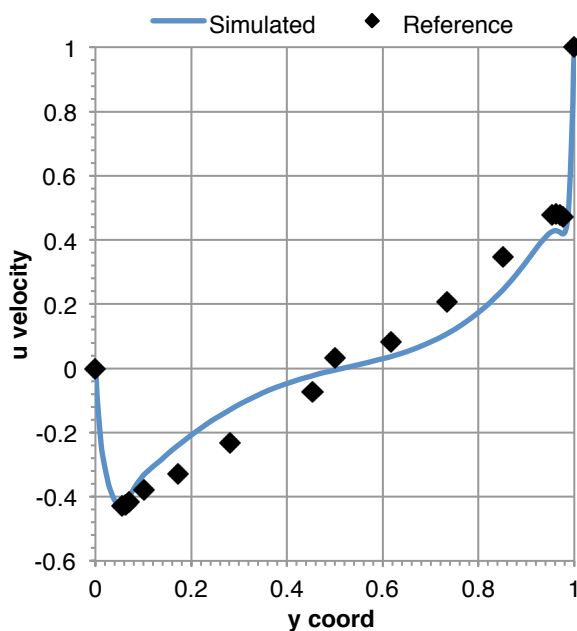
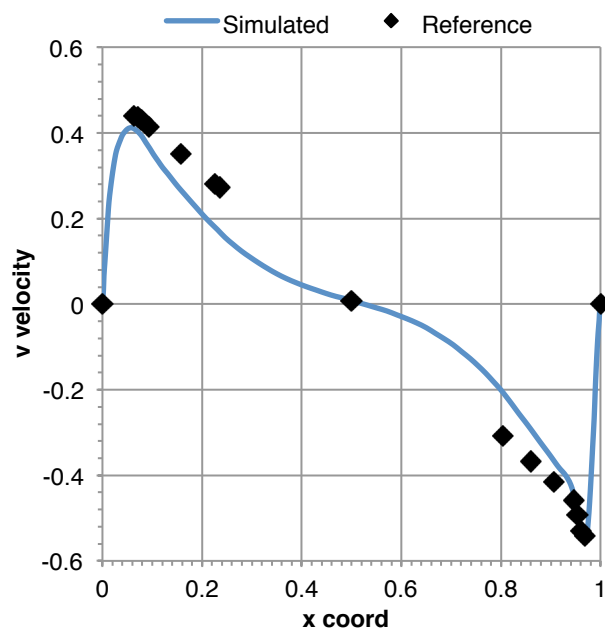
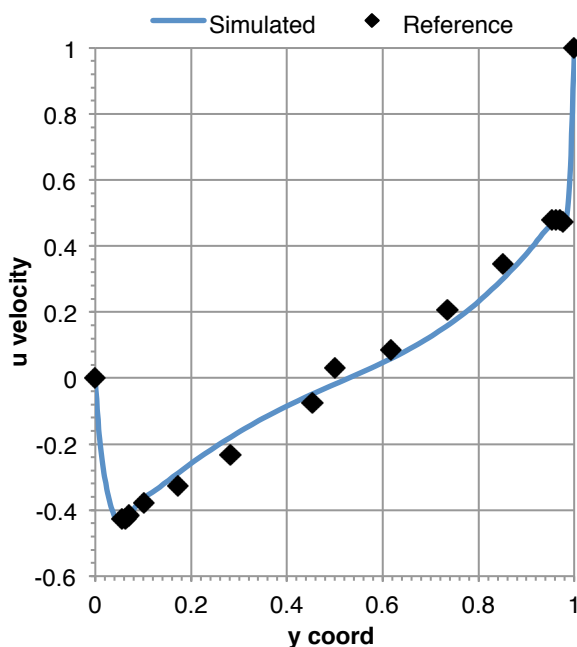
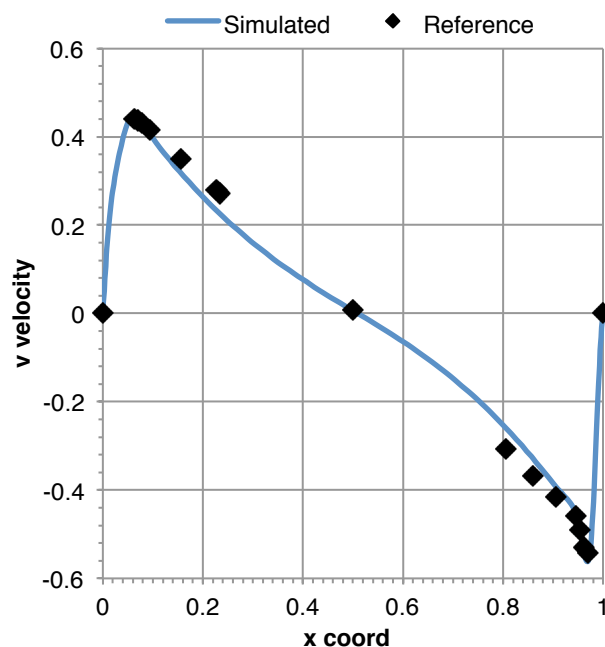


Figure 3.12: Centerline velocities comparison at $Re = 7.500$

Centerline velocities at Re=10000**100 x 100 element mesh****Figure 3.13:** Centerline velocities comparison at $Re = 10.000$ **Centerline velocities at Re=10000****120 x 120 element mesh****Figure 3.14:** Centerline velocities comparison at $Re = 10.000$ using a denser mesh

As it can be seen from figures in the previous pages, the simulated results obtained with the self-developed code and the reference values match almost perfectly up to $Re = 5000$ (Figure 3.7 to Figure 3.11). However, some divergence between the results appear for $Re = 7.500$ (Figure 3.12) and the effect is much more appreciable for $Re = 10.000$ (Figure 3.13), where differences start to become important.

The code developed tries to reach a steady state comparing the results obtained in the previous time-step with the last ones calculated. This means that if the flow is completely laminar, the steady state can be achieved and the iterative process will stop. Nevertheless, if the flow starts to become turbulent in some areas, the chaotic and non-steady nature of turbulence will prevent the code to reach numerical convergence in time.

For the higher values of Reynolds number simulated, there is some discussion if the flow of the cavity remains steady or not. The simulations carried out using a 100×100 element refined mesh for Reynolds values of 7.500 and 10.000 were not able to reach steady state convergence with the same precision used in the other Reynolds values. In order to overcome this drawback, a denser mesh can be a proper solution. In Figure 3.14, a 120×120 element mesh is used instead of a 100×100 and it can be appreciated that there is a significant improvement and the results tend to match the reference values.

However, the computational time to obtain this improved solution is about a 50% higher than the other one. Dealing with more control volumes does not only mean to do more calculations at every time iteration, but to increase also the number of time-steps. The fact of using a smaller grid forces the numerical scheme to use also smaller time-step for numerical stability reasons, as the code uses a fully explicit scheme and CFL condition must be fulfilled. In other words, a denser mesh means much more computer power and time that are not available with the current resources.

Nevertheless, the results obtained for low Reynolds numbers are good enough so the conclusion is that the code is able to solve laminar flows with good accuracy.

In the following pages there are some examples of the flow configuration obtained with the numerical code for different Reynolds numbers.

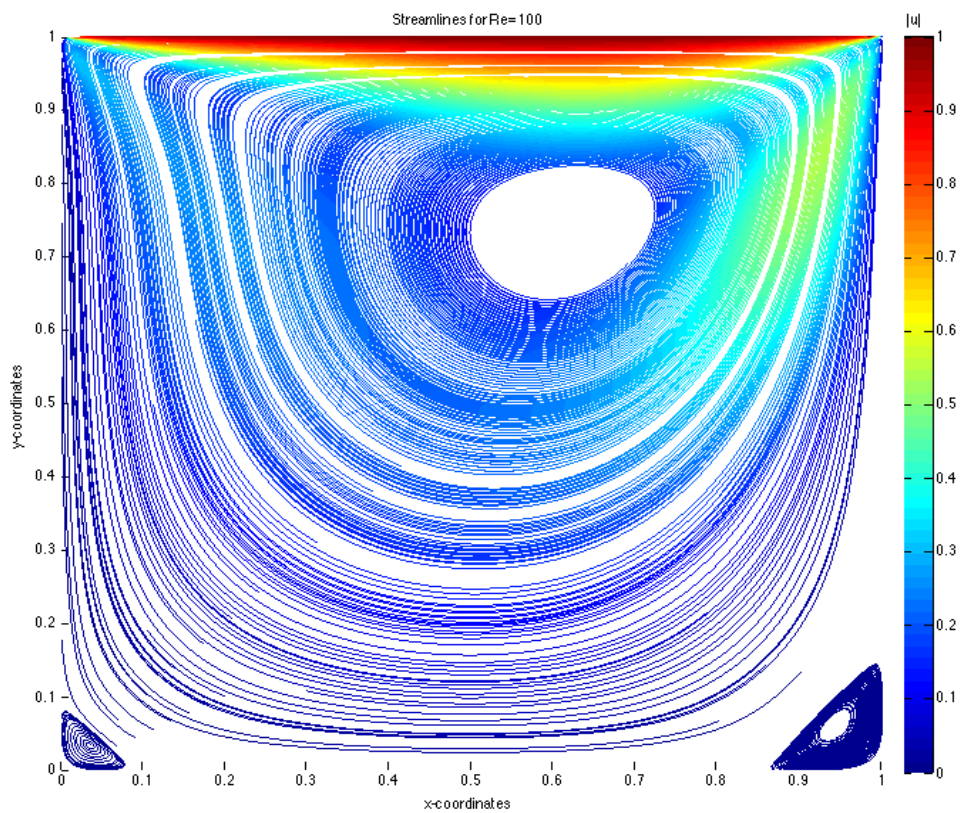


Figure 3.15: Streamlines for $Re=100$

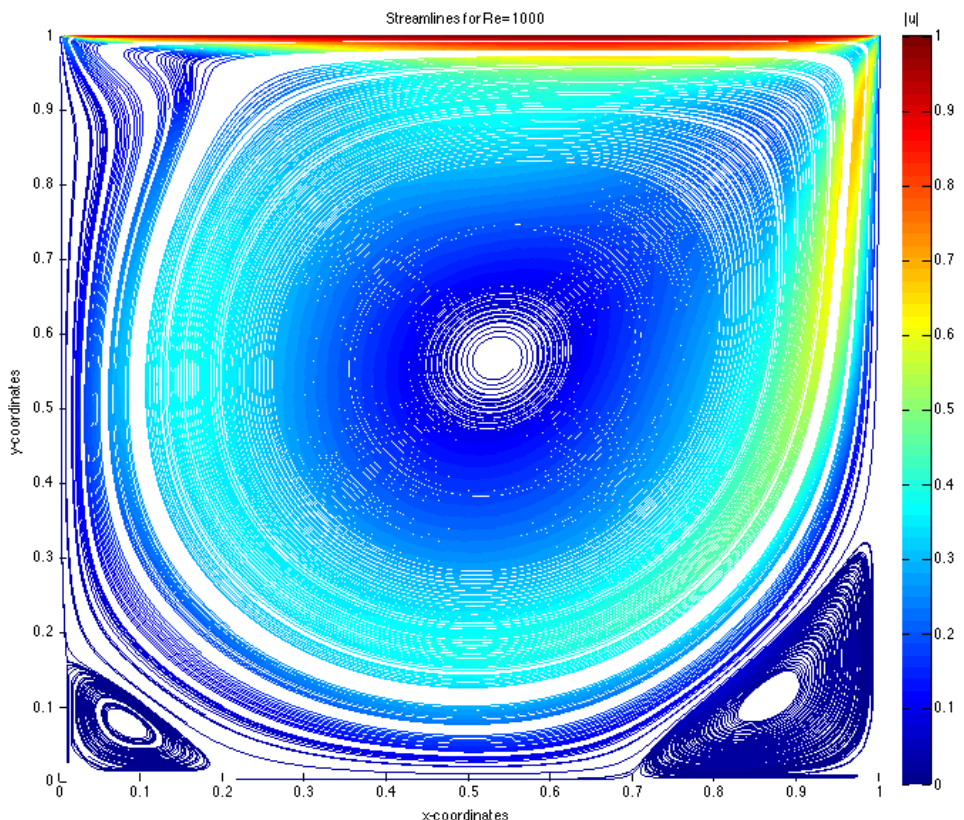


Figure 3.16: Streamlines for $Re=1.000$

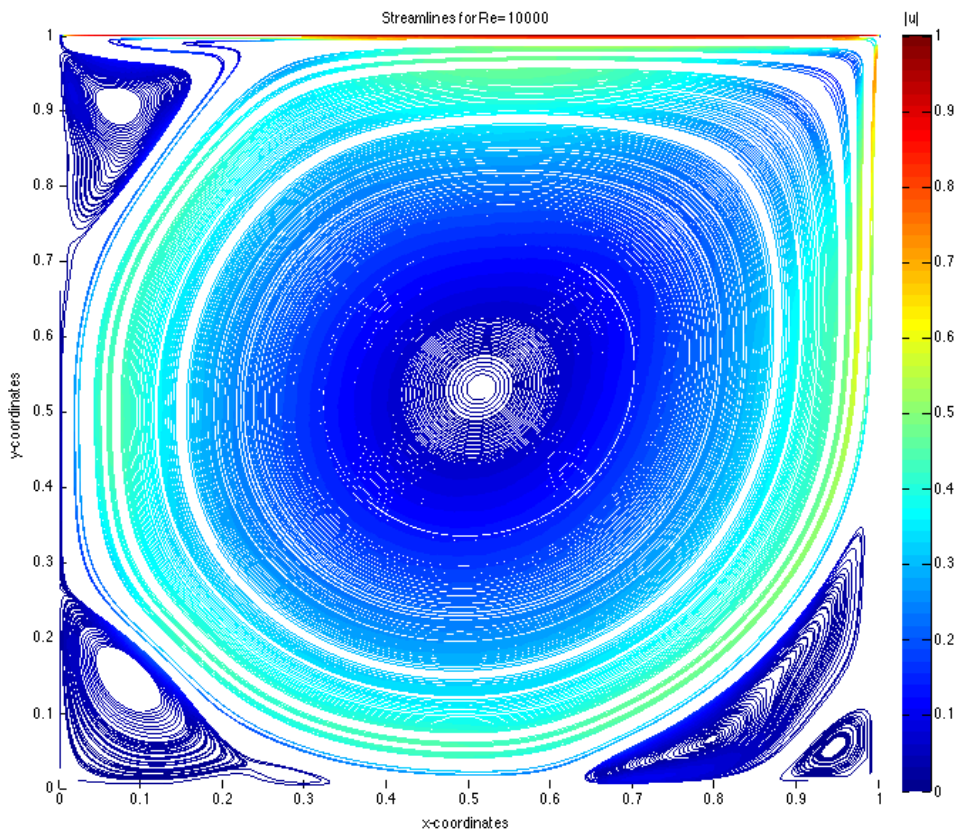


Figure 3.17: Streamlines for $Re=10.000$

In the previous figures there is a graphical example of the difference that the flows presents when the Reynolds number is increased. Notice that the little eddies that appear on the lower corners for the case of $Re=100$ are much more developed in for a value of $Re=1000$. In the last figure, where the flow is almost turbulent, a new vortex appear in the upper left side and in the lower right side the vortex is split in two.

The configuration of the flow that can be seen in the plots matches with good accuracy the plots presented by [17] in position and size of the vortex. More images for different regimes and variables can be found in ANNEX A SECTION 1.

3.4 Differentially heated cavity

Differentially heated cavity is a case of natural convection. It consists of a fluid enclosed in square cavity that is heated from one of the sidewalls. In this case, left wall is the hot wall and right wall is the cold wall, whereas top and bottom walls are adiabatic. To study the flow in the cavity, the three equations (continuity, momentum and energy) have to be solved. The solution obtained for different values of Ra number is then compared to the benchmark solution presented in [19] and [20].

3.4.1 Governing equations and parameters

As it has been said, to solve the differentially heated cavity problem it is necessary to solve the three equations introduced in 2.1. Unlike the driven cavity problem, as this is a natural convection problem there is not an external velocity responsible for driving the flow. Instead, the difference of density when the fluid is heated is what produces the “natural” motion of the fluid. In order to represent this phenomenon the Boussinesq hypothesis will be applied.

Remember that the code developed until now is for incompressible fluids, which means that is not able to deal with a variable density. However, the Boussinesq hypothesis stands that for low Mach numbers, where compressibility is not important, the variations of density can be neglected except in the terms where it is multiplied by the gravity, which is strong enough to produce some variations in the flow.

It is considered that in the regimes simulated the variations of density are only affected by temperature but not pressure. These variations are related with the expansion coefficient of the fluid

$$\beta = -\frac{1}{\rho} \left(\frac{\partial \rho}{\partial T} \right)_{p_0} \quad (3.28)$$

Introducing this term to the dimensionless equations one can obtain the following set of PDE's [19], [21], [22]

$$\nabla \cdot \mathbf{u} = 0 \quad (3.29)$$

$$\frac{\partial \mathbf{u}}{\partial t} + (\mathbf{u} \cdot \nabla) \mathbf{u} = Pr \Delta \mathbf{u} - \nabla p + \mathbf{f} \quad (3.30)$$

$$\frac{\partial T}{\partial t} + (\mathbf{u} \cdot \nabla) T = \nabla^2 T \quad (3.31)$$

Where \mathbf{u} is the dimensionless velocity vector, p is the dimensionless pressure and T is the dimensionless temperature. \mathbf{f} is the body forces term and its value is the following

$$\mathbf{f} = (0, RaPrT) \quad (3.32)$$

It can be seen that it only has a single component in the vertical direction. This is because the only body force taken into account is the gravity, as it was specified in 2.1.2, and it only has components in this direction.

Ra and Pr are the dimensionless Rayleigh and Prandtl numbers, respectively, and they are defined in the following way [19]

$$Ra = \frac{g\beta L^3 \Delta T}{\nu\alpha} \quad (3.33)$$

$$Pr = \frac{\nu}{\alpha} \quad (3.34)$$

Where g is the gravity acceleration, β is the expansion coefficient of the fluid, L is the characteristic length of the cavity, ΔT is the temperature difference between the hot and cold walls, ν is the kinematic viscosity of the fluid and α is the thermal conductivity of the fluid. For air, the fluid that will be simulated, the Prandtl number has an approximated value of $Pr = 0,71$. As in the driven cavity problem, the characteristic length and the temperature difference are set to $\Delta T = L = 1$ and with Pr also defined, the rest of the values are defined to match the Ra that is going to be simulated.

3.4.2 Boundary conditions

For velocity and pressure the boundary conditions are very similar to the ones used in the driven cavity problem. The main difference is that in this case the no-slip condition for velocity is applied at the four walls, so the pressure gradient will be also 0 at every wall

$$u = 0, v = 0 \quad \text{at all walls} \quad (3.35)$$

$$\frac{\partial p}{\partial y} = 0 \quad \text{at } y = 0, y = 1; x \in (0,1) \quad (3.36)$$

$$\frac{\partial p}{\partial x} = 0 \quad \text{at } x = 0, x = 1; y \in (0,1) \quad (3.37)$$

The new constrain that has to be taken into account in this problem is related with temperature. As explained, the domain consists of a hot wall, a cold wall and the rest are adiabatic. As the difference of temperatures $\Delta T = T_H - T_C$ is taken as reference and set to $\Delta T = 1$, the hot and cold temperatures have to fulfil this constrain. For the adiabatic walls, the heat flux has to be set to 0 and this means to cancel the derivative of temperature in the perpendicular direction towards the wall. To sum up, the temperature boundary conditions are

$$T_H = 1 \quad \text{at } x = 0; y \in (0,1) \quad (3.38)$$

$$T_C = 0 \quad \text{at } x = 1; y \in (0,1) \quad (3.39)$$

$$\frac{\partial T}{\partial y} = 0 \quad \text{at } y = 0, y = 1; x \in (0,1) \quad (3.40)$$

These are all the conditions that have to be taken into account to carry out the simulation of the differentially heated cavity problem.

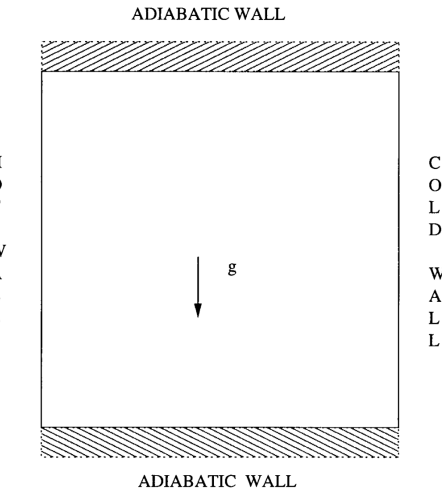


Figure 3.18: Representation of the domain. Extracted from [23]

3.4.3 Numerical method

In this case, the simulations are carried out using structured uniform meshes with different grid spacing in order to compare the results obtained with both.

Convective and diffusive terms are evaluated using the same second-order CDS scheme and an explicit scheme is used for time discretization. In this case, besides the pressure-velocity coupling, there is also a temperature-velocity coupling as the Boussinesq hypothesis adds a temperature dependant term to the momentum equation.

To solve both couplings, fractional step method is applied. For simplifying the notation, equations 3.30 and 3.31 can be rewritten as follows

$$\frac{\partial \mathbf{u}}{\partial t} = R(\mathbf{u}, \mathbf{f}) - \nabla p \quad (3.41)$$

$$\frac{\partial T}{\partial t} = R(\mathbf{u}, T) \quad (3.42)$$

Where $R(\mathbf{u}, \mathbf{f}) = -(\mathbf{u} \cdot \nabla) \mathbf{u} + Pr \Delta \mathbf{u} - \nabla p + \mathbf{f}$ and $R(\mathbf{u}, T) = -(\mathbf{u} \cdot \nabla) T + \nabla^2 T$. These two terms are evaluated and discretized in space in the same way than in the Driven Cavity problem explained in 3.3.3. For the time discretization a fully explicit second-order Adams-Bashforth scheme is used and the equations are

$$\frac{\mathbf{u}^{n+1}-\mathbf{u}^n}{\Delta t} = \frac{3}{2} R(\mathbf{u}, \mathbf{f})^n - \frac{1}{2} R(\mathbf{u}, \mathbf{f})^{n-1} - \nabla p^{n+1} \quad (3.43)$$

$$\frac{T^{n+1}-T^n}{\Delta t} = \frac{3}{2} R(\mathbf{u}, T)^n - \frac{1}{2} R(\mathbf{u}, T)^{n-1} \quad (3.44)$$

$$\nabla \cdot \mathbf{u}^{n+1} = 0 \quad (3.45)$$

The new temperature field T^{n+1} is obtained directly from equation 3.44 but the velocity field \mathbf{u}^{n+1} is calculated using the FSM. The methodology is the same used in the Driven Cavity problem, obtaining the predictor velocity in first place and then solving the Poisson equation for pressure.

The explicit scheme used it also needs to fulfil the constrain marked by the CFL condition in the value of the time-step for numerical stability reasons.

3.4.4 Results

The simulations have been carried out for different values of the Rayleigh number, 10^3 , 10^4 , 10^5 and 10^6 . The fluid used is air with a Prandtl number value of $Pr = 0,71$. The results from these simulations are compared with the benchmark results in the following pages.

The values compared are related with the modulus of the velocity components and the dimensionless Nusselt number, which is related with the dimensionless heat flux that is transferred and it is a parameter of significant importance in engineering problems. As in the simulation all the variables are defined in its dimensionless form, the local Nusselt number at the vertical hot wall is defined as [22]

$$Nu_y = -\left. \frac{\partial T}{\partial x} \right|_{x=0} \quad (3.46)$$

Then, the overall averaged Nusselt number at the hot wall can be written as

$$Nu_0 = \frac{1}{H} \int_0^H -\frac{\partial T}{\partial x} dy \quad (3.47)$$

In the following tables, the simulation results are presented for different mesh sizes and are compared to the benchmark showing the percentage of deviation between the two results. The values compared are the following ones:

Nu_0 : overall averaged Nusselt number at the hot wall.

Nu_{max} : maximum value of the local Nusselt number at the hot wall, with its position.

Nu_{min} : minimum value of the local Nusselt number at the hot wall, with its position.

u_{max} : maximum u velocity value at the vertical centreline of the cavity, with its position.

v_{max} : maximum v velocity value at the horizontal centreline of the cavity, with its position.

$Ra = 10^3$							
	Benchmark	40x40	error [%]	60x60	error [%]	80x80	error [%]
Nu_0	1.117	1.120	0.250 %	1.118	0.125 %	1.118	0.090 %
Nu_{max}	1.505	1.512	0.465 %	1.509	0.266 %	1.508	0.199 %
y	0.092	0.088	4.348 %	0.075	18.478 %	0.081	11.957 %
Nu_{min}	0.692	0.690	0.289 %	0.690	0.289 %	0.691	0.145 %
y	1.000	0.988	1.200 %	0.992	0.800 %	0.981	1.900 %
u_{max}	3.649	3.657	0.219 %	3.651	0.058 %	3.649	0.008 %
y	0.813	0.812	0.062 %	0.808	0.574 %	0.819	0.707 %
v_{max}	3.697	3.699	0.041 %	3.700	0.089 %	3.699	0.046 %
x	0.178	0.188	5.337 %	0.175	1.685 %	0.181	1.826 %

Table 3.2: Results comparison for $Ra=1e3$

$Ra = 10^4$							
	Benchmark	40x40	error [%]	60x60	error [%]	80x80	error [%]
Nu_0	2.238	2.260	0.983 %	2.251	0.581 %	2.249	0.492 %
Nu_{max}	3.528	3.583	1.559 %	3.554	0.737 %	3.544	0.454 %
y	0.143	0.138	3.497 %	0.142	0.699 %	0.144	0.699 %
Nu_{min}	0.586	0.584	0.341 %	0.584	0.341 %	0.585	0.171 %
y	1.000	0.988	1.200 %	0.992	0.800 %	0.994	0.600 %
u_{max}	16.178	16.143	0.216 %	16.183	0.031 %	16.18	0.012 %
x	0.823	0.812	1.276 %	0.825	0.243 %	0.819	0.516 %
v_{max}	19.617	19.636	0.097 %	19.603	0.071 %	19.64	0.097 %
x	0.119	0.113	5.462 %	0.125	5.042 %	0.119	0.210 %

Table 3.3: Results comparison for $Ra=1e4$

$Ra = 10^5$							
	Benchmark	40x40	error [%]	60x60	error [%]	80x80	error [%]
Nu_0	4.509	4.623	2.528 %	4.567	1.286 %	4.547	0.843 %
Nu_{max}	7.717	8.189	6.116 %	7.936	2.838 %	7.841	1.607 %
y	0.081	0.062	23.45 %	0.075	7.407 %	0.081	0.000 %
Nu_{min}	0.729	0.720	1.235 %	0.725	0.549 %	0.726	0.412 %
y	1.000	0.988	1.200 %	0.992	0.800 %	0.994	0.600 %
u_{max}	34.730	34.831	0.291 %	34.799	0.199 %	34.780	0.144 %
y	0.855	0.863	0.877 %	0.858	0.389 %	0.856	0.146 %
v_{max}	68.590	69.027	0.637 %	68.336	0.370 %	68.611	0.031 %
x	0.066	0.062	5.303 %	0.058	11.62 %	0.069	4.167 %

Table 3.4: Results comparison for $Ra=1e5$

$Ra = 10^6$							
	Benchmark	40x40	error [%]	60x60	error [%]	80x80	error [%]
Nu_0	8.817	9.426	6.907 %	9.101	3.221 %	8.982	1.871 %
Nu_{max}	17.925	20.494	14.33 %	19.451	8.513 %	18.735	4.519 %
y	0.038	0.038	0.529 %	0.025	33.86 %	0.031	17.99 %
Nu_{min}	0.989	0.938	5.157 %	0.963	2.629 %	0.970	1.921 %
y	1.000	0.988	1.200 %	0.992	0.800 %	0.994	0.600 %
u_{max}	64.630	65.922	1.999 %	65.433	1.242 %	65.180	0.851 %
x	0.850	0.863	1.471 %	0.858	0.980 %	0.856	0.735 %
v_{max}	219.360	223.680	1.969 %	219.650	0.132 %	218.460	0.410 %
x	0.038	0.037	1.055 %	0.042	9.939 %	0.031	17.55 %

Table 3.5: Results comparison for $Ra=1e6$

The results from the previous tables clearly show two tendencies. The first one is that the results are improved when a denser mesh is used. Obviously this is the expected behaviour and in Figure 3.19 it can be seen that the error for Nu_0 follows the 2-slope line, what agrees with the use of a second-order CDS scheme.

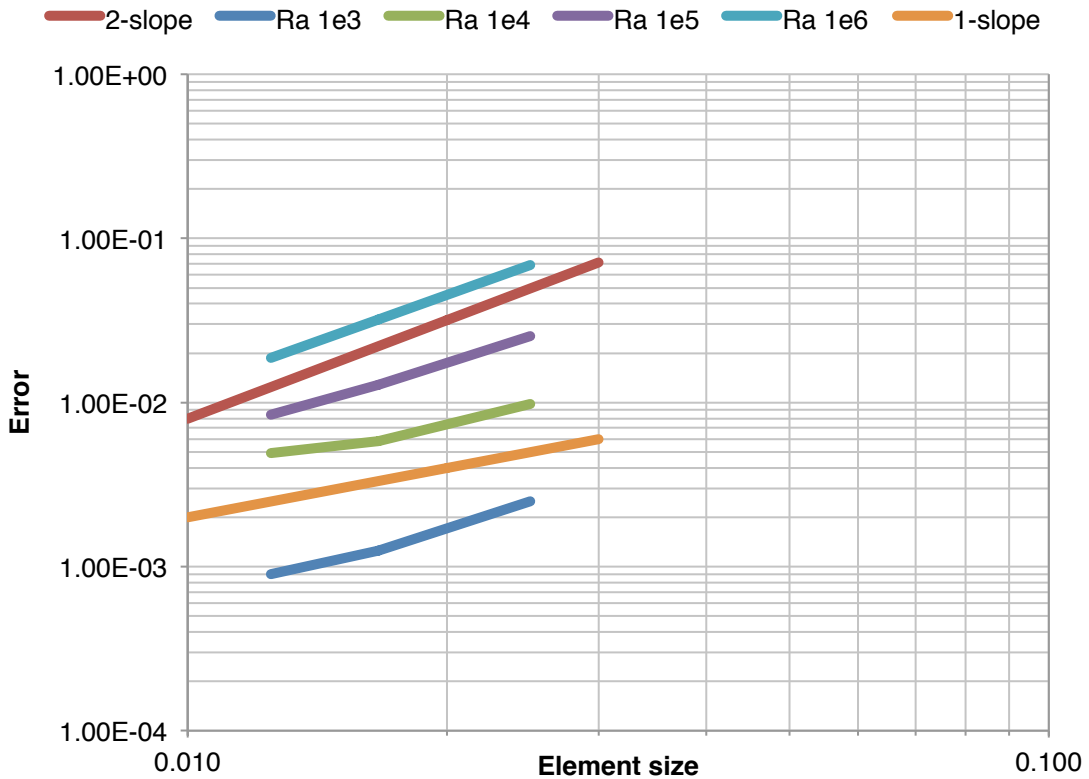


Figure 3.19: Numerical error of Nu_0 versus element size

Notice that the slope is slightly higher for the high Rayleigh number values and it is related with the more turbulent nature of the flow as the Rayleigh number increases. Coarser meshes have more difficulty to represent turbulent flows and a higher error is committed using them.

The relation between the resolution of the mesh and the Rayleigh number of the simulation can also be seen observing the absolute value of the error. All the values studied show a bigger error for higher Rayleigh numbers regardless of the mesh size. This fact can also be seen graphically in Figure 3.19 as the lines for the higher Rayleigh numbers are above the ones for the lowest.

Overall, the conclusion that can be extracted from this benchmark test is that the numerical solutions obtained with the self-developed code certainly agree with the benchmark solutions and their behaviour is the expected. The biggest discrepancies are related with the position of the extreme values. One of the reasons for this imbalance is the fact that the values of the benchmark solution are obtained using an interpolation

from the discrete numerical solution while the presented values are directly derived from the discrete ones.

In the following pages some output of the numerical code is presented like streamline and isotherm plots for different Ra numbers. In the figures, the evolution of the flow as it becomes more turbulent can be clearly seen.

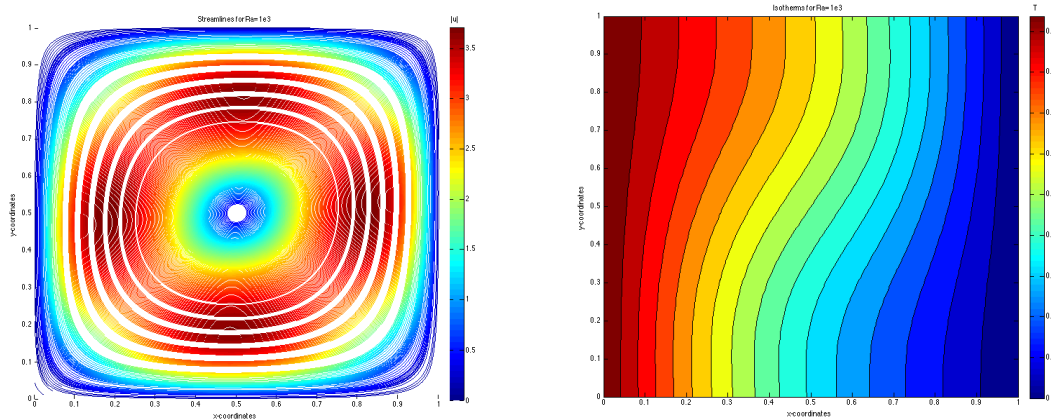


Figure 3.20: Streamlines (left) and isotherms (right) for $Ra=1e3$

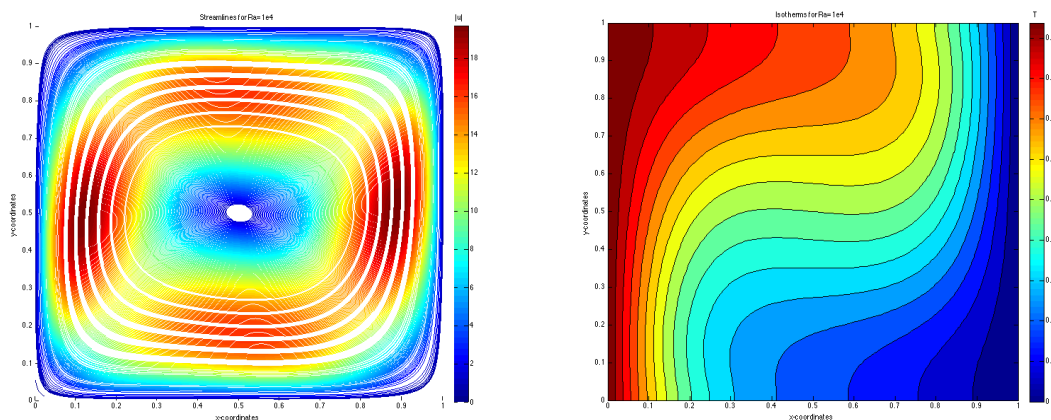


Figure 3.21: Streamlines (left) and isotherms (right) for $Ra=1e4$

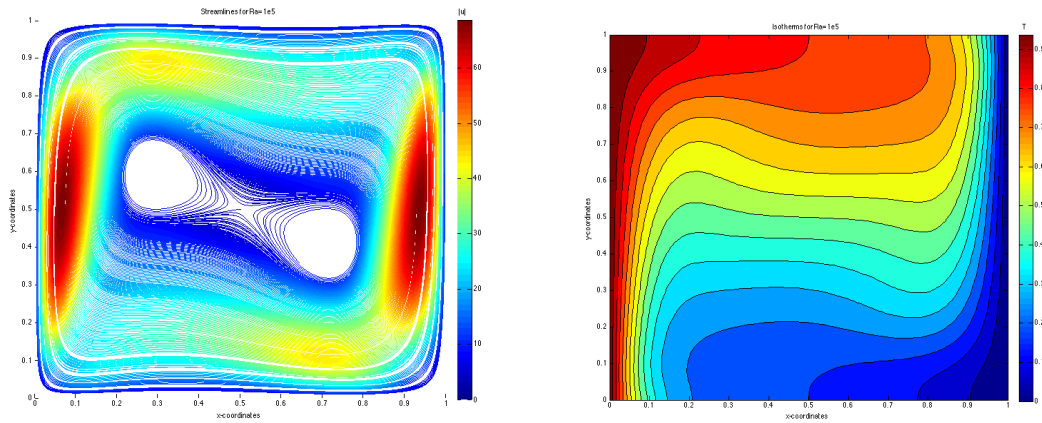


Figure 3.22: Streamlines (left) and isotherms (right) for $Ra=1e5$

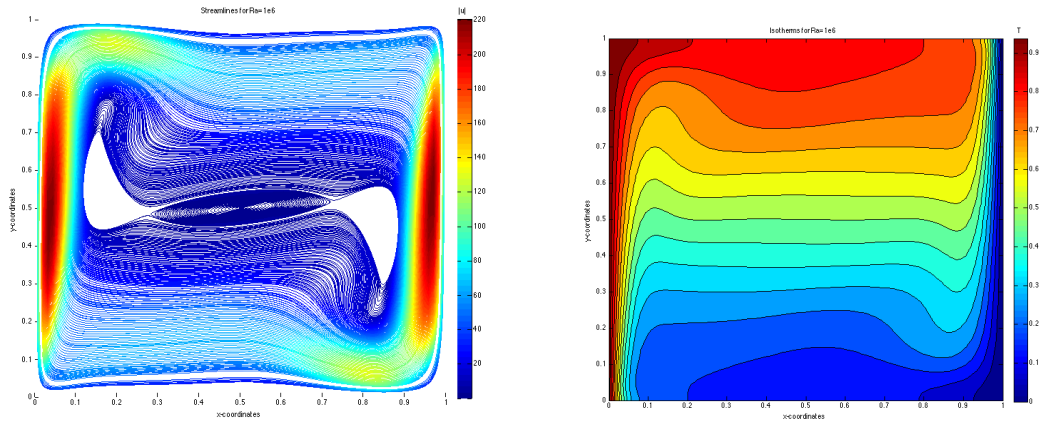


Figure 3.23: Streamlines (left) and isotherms (right) for $Ra=1e6$

It can be seen that the temperature near the hot wall and the difference in density is what triggers the movement of the fluid. The velocity achieves its higher values near the walls while the centre of the cavity remains practically at rest.

The flow configurations and the distribution of temperatures are very similar to the ones presented by [20] or [23] so the conclusion that can be extracted is that the code is solving the problem in the right way. For more information about the output data see ANNEX A SECTION 2.

4 Vortex-induced vibrations

In this part of the study, the main objective is to use the self-developed numerical software to work on a case that has possible real applications, which in fact is the main purpose of any CFD code.

The field of study is limited to the capabilities of the software that in this case include the possibility to simulate incompressible laminar flows. This fact narrows the potential cases as for example in aerodynamics the Reynolds numbers involved in most of the cases are of several orders of magnitude higher than the ones tested in the benchmark simulations. However, for low velocities and small geometries, which involves low Reynolds numbers, the self-developed code should work properly and the case studied in this chapter goes in that direction, studying the flow past square cylindrical structures in low Reynolds numbers.

4.1 Definition of the phenomena

In fluid dynamics there is an interesting phenomena that appears after a flow past a bluff body at certain velocities. This flow is characterized for a massive separated region downstream of the obstacle in which alternating low-pressure vortices appear. These vortices detach periodically from the backside and create an oscillating force on the object. The periodic phenomenon is referred as vortex shedding as well as the antisymmetric wake flow pattern is known as Kármán vortex street [24].

For determined regimes, the vortices that detach from the obstacle have a very characteristic frequency. At the same time, this fact is inducing a force on the structure with the same features that can lead to structural problems if it matches with the natural frequency of the structure.

The effect is found in different engineering fields like high buildings, towers, chimneys, bridges or wires. If the conditions are such favourable for the vibration phenomenon, the whole structure is likely to suffer a collapse. It also has importance on the transportation of energy by the flow and can affect the temperature distribution downstream [25].

A common approach used in fluid dynamics to study different flows and geometries is the utilization of dimensionless parameters such as the Reynolds number that characterised the flow in the driven cavity or the Rayleigh number in the differentially heated cavity. In the cases where vortex shedding is involved, the two key parameters are the Reynolds number and the Strouhal number.

The Reynolds number represents a ratio between inertial and viscous forces, which is closely related to the turbulence or laminar nature of the flow. In the case of an obstacle in a free stream the Reynolds number is defined as

$$Re = \frac{\rho U_\infty L}{\mu} \quad (4.1)$$

Where ρ is the density of the fluid, U_∞ is the free stream velocity upstream of the obstacle, μ is the dynamic viscosity of the fluid and L is the characteristic length of the obstacle. This parameter could be either the diameter of a cylinder or the length of a rectangular geometry.

The Strouhal number is related with oscillating flows and Vincenc Strouhal proposed it in 1878 when he was experimenting with wires experiencing vortex shedding and singing in the wind. The number is defined as

$$St = \frac{fL}{U_\infty} \quad (4.2)$$

Where f is the frequency of vortex shedding, L is the characteristic length of the object (defined as in Re) and U_∞ is the velocity upstream of the obstacle.

Studying the flow and the influence of these two parameters will help to understand the phenomenon and to take into consideration the possible affections to the components that suffer it.

4.2 Governing equations and numerical method

In this section there is a brief explanation of the mathematical background and the methods used to solve the problem.

4.2.1 Governing equations

In a first approximation it is considered that there is no heat transfer in the domain so momentum and continuity equations are taken into account in its dimensionless form

$$\nabla \cdot \mathbf{u} = 0 \quad (4.3)$$

$$\frac{\partial \mathbf{u}}{\partial t} + (\mathbf{u} \cdot \nabla) \mathbf{u} = \frac{1}{Re} \Delta \mathbf{u} - \nabla p \quad (4.4)$$

Where \mathbf{u} is the dimensionless velocity vector, Re is the Reynolds number and p is the dimensionless pressure. It can be seen that the equations are the same that in the driven cavity case and so the assumptions taken.

The net force that the obstacle is suffering is equal to the integral of the surface forces along the boundary of the object and it has to different origins, the pressure differences and the viscous stresses [26]

$$\mathbf{F} = \int p \cdot ds + \int \tau \cdot ds \quad (4.5)$$

Where p is the pressure distribution and τ is the viscous stress distribution. To make things easy, this force is usually decomposed into two components, lift and drag, one perpendicular and the other parallel to the free stream direction.

Lift is the component of the force perpendicular to the free stream direction and in aviation is responsible for maintaining planes in the air. In the case of study the lift force can be split in four terms, each one of them corresponds to a different face of the rectangular obstacle and it has to be integrated along each face

$$L = \int_s p \, dx - \int_n p \, dx + \mu \int_e \frac{\partial v}{\partial x} dy + \mu \int_w \frac{\partial v}{\partial x} dy \quad (4.6)$$

Drag is the component of the force parallel to the free stream direction and it represents the opposition that the fluid imposes to any body placed inside a stream. The same procedure of calculation is applied here

$$D = \mu \int_s \frac{\partial u}{\partial y} dx + \mu \int_n \frac{\partial u}{\partial y} dx - \int_e p \, dy + \int_w p \, dy \quad (4.7)$$

The surfaces n, s, e and w refers to the walls north, south, east and west of the object following the same nomenclature than the used for the finite volumes.

As any other variable involved in the problem, the forces have to be dimensionless. To do so the dynamic pressure of the free stream and a reference length are used, which results in two well known coefficients in aerodynamics terminology [26]

$$C_l = \frac{L}{\frac{1}{2} \rho U_\infty c_{ref}} \quad (4.8)$$

$$C_d = \frac{D}{\frac{1}{2} \rho U_\infty c_{ref}} \quad (4.9)$$

Where ρ is the density of the fluid, U_∞ is the free stream velocity and c_{ref} is a characteristic length of the object that is analysed.

4.2.2 Numerical method

As it has been explained, the equations that have to be solved are the same than in the driven cavity case. Continuity and momentum equations are characterised by the velocity-pressure coupling that in this case is solved in the same way using a FSM. In sections 3.3 and 3.4 there is a quite extended explanation of the different steps that have to be followed to implement the FSM so the reader can find more details on the calculation of the predictor velocities or the solving of the Poisson equation for pressure in the indicated sections.

The time discretization follows the same Adams-Bashforth fully explicit scheme and the time step fulfils the CFL condition. Both convective and diffusive terms are evaluated using a second-order CDS scheme.

What is new, in respect to the benchmark cases, is the calculation of the aerodynamic forces. The calculation of pressure difference between two opposite walls of the object is straightforward as the pressure field is solved for each time-step and the evaluation of the velocity gradient is done in the same way than in the diffusive term, using a central difference second-order approximation.

4.3 Geometry and boundary conditions

In the following section there is a brief description of the geometry of the problem and the mesh used as well as the boundary conditions applied to the different variables.

In real world a flow like the one that is being studied has a nearly infinite domain and is not affected by other perturbations but the obstacle itself. However, it is impossible to simulate an infinitely large domain using numerical methods so the approach that is followed is to confine the flow in a rectangular channel, with an inlet and an outlet, where the obstacle is placed like what would be done in a real wind tunnel. The geometry and the boundary conditions have to be the right ones to ensure that the finite domain does not affect the flow in the sections of study.

4.3.1 Mesh and geometry

The geometry of the problem is quite simple and it depends on few parameters that can be seen in Figure 4.1

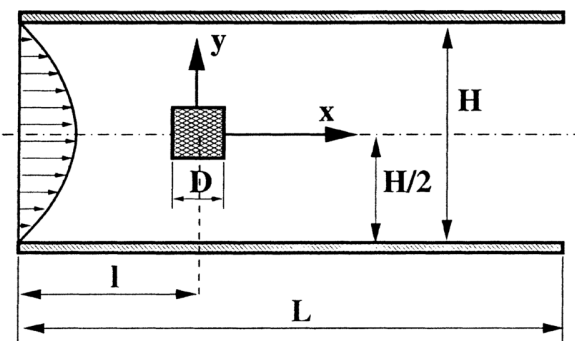


Figure 4.1: Graphic representation of the domain and the obstacle. Extracted from: [27]

D is the diameter of the square cylinder, H the height of the channel, L the length of the channel and l the distance between the inlet and the obstacle. As explained in [24] there is some discussion on the relations between the different geometric parameters in order to not affect the flow that is being studied. The blockage ratio, defined as $\beta = \frac{D}{H}$, and the distance between the obstacle and the inlet and the outlet are crucial to prevent the flow to be affected. The values recommended by [27] are the following

- Blockage ratio: $\beta = \frac{1}{8}$
- Length of the channel: $L = 50 \cdot D$
- Distance to the inlet: $l = L/4$

In first approach this will be the ratios used to the simulations.

Another interesting point is the mesh. The fact of defining a domain that is large enough to not affect the flow has a potential drawback because the part that is not interesting to be studied has to be also solved using iterative methods and consuming computer power. A proper solution to this problem is to use a refined mesh that concentrates the control volumes in the zones near the obstacle.

To make things easy, this concentration of control volumes is only applied along the parallel direction to the x-axis, as the longitude is much bigger than the height and the perturbations in the vertical direction occupy a larger portion of the domain.

To do so, the total number of control volumes is defined as well as the number of control volumes that will be concentrated in a finer uniform mesh around the point where the object is placed. Then a hyperbolic tangent function is used to distribute the remaining control volumes proportionally towards the inlet and the outlet, making these ones bigger as they move away of the obstacle. An example of the mesh that is used in the simulations can be seen in Figure 4.2 with the obstacle painted in red

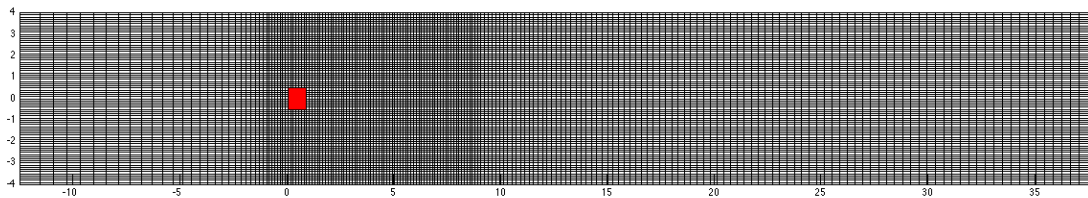


Figure 4.2: Example of the mesh used in the simulations.

From the figure it is clear which is the region of interest to be studied and how the control volumes are distributed along the domain.

4.3.2 Boundary conditions

Unlike what happened in the benchmark cases where the fluid was enclosed in a cavity, in this case the code has to deal with an open system where the mass flow at the inlet has to be the same than the mass flow at the outlet.

For this reason, boundary conditions have to be treated specifically in the inlet and the outlet as well as the other walls. There is some discussion in the literature about which are the best boundary conditions as it can be seen in [27], [24] or [28].

4.3.2.1 Wall conditions

The non-slip condition is applied to the upper and bottom walls of the channel, the same condition applied in the driven cavity problem. The velocity components have fixed values and the pressure gradient is set to 0

$$u = 0, v = 0 \quad \text{at } y = -\frac{H}{2}, y = \frac{H}{2}; x \in (0, L) \quad (4.10)$$

$$\frac{\partial p}{\partial y} = 0 \quad \text{at } y = -\frac{H}{2}, y = \frac{H}{2}; x \in (0, L) \quad (4.11)$$

4.3.2.2 Inlet conditions

At the inlet the incoming flow velocity is fixed. To avoid the appearance of vortices near the wall due to high velocity gradients, a parabolic profile is used. The pressure gradient in the horizontal direction is also set to 0.

$$u = [1 - (2\beta y)^2], v = 0 \quad \text{at } x = 0; y \in \left(-\frac{H}{2}, \frac{H}{2}\right) \quad (4.12)$$

$$\frac{\partial p}{\partial x} = 0 \quad \text{at } x = 0; y \in \left(-\frac{H}{2}, \frac{H}{2}\right) \quad (4.13)$$

4.3.2.3 Outlet conditions

At the outlet the conditions that seems to work better is the convective boundary condition, which has the following expression

$$\frac{\partial U_i}{\partial t} + U_C \frac{\partial U_i}{\partial x} = 0 \quad (4.14)$$

Where U_C is the convective velocity and following the recommendation from [28] its value is set to $\frac{2}{3} U_\infty$, which is the average streamwise velocity. In the numerical scheme, the boundary condition is implemented to the boundary nodes as

$$U_N^{n+1} = U_N^n - \frac{\Delta t}{(\Delta x)_N} U_C (U_N^n - U_{N-1}^n) \quad (4.15)$$

Where N refers to the streamwise grid number at the outlet and n to the time-step. The convective boundary is applied to both horizontal and vertical velocities. The pressure gradient in the horizontal direction is set to 0.

4.4 Results

4.4.1 Steady flow

For very low Reynolds the flow does not present any periodic oscillation downstream of the obstacle. The flow is completely laminar and steady and the figures show that there is no detachment of the flow downstream the obstacle.

When the Reynolds number is increased, the flow continues to be steady but a recirculation zone appears in the back face of the obstacle. The length of this recirculation zone increases with the Reynolds number as it can be seen in Figure 4.3 and Figure 4.4. Reference values from [27]. More graphic information can be found at ANNEX A SECTIONS 3.1 to 3.6.

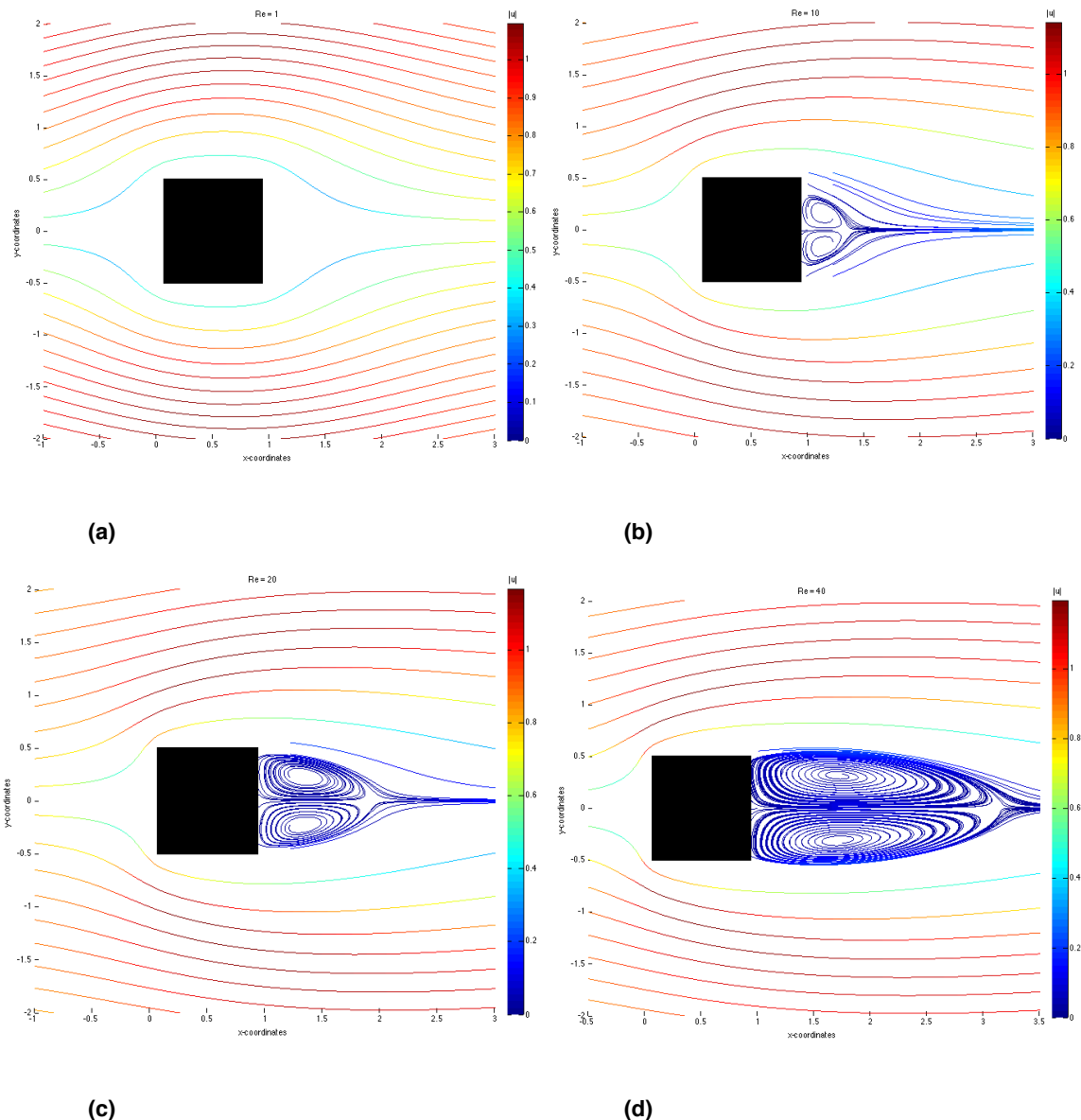


Figure 4.3 Streamlines around the cylinder for different Re numbers. a) $Re=1$ b) $Re=10$ c) $Re=20$ d) $Re=40$

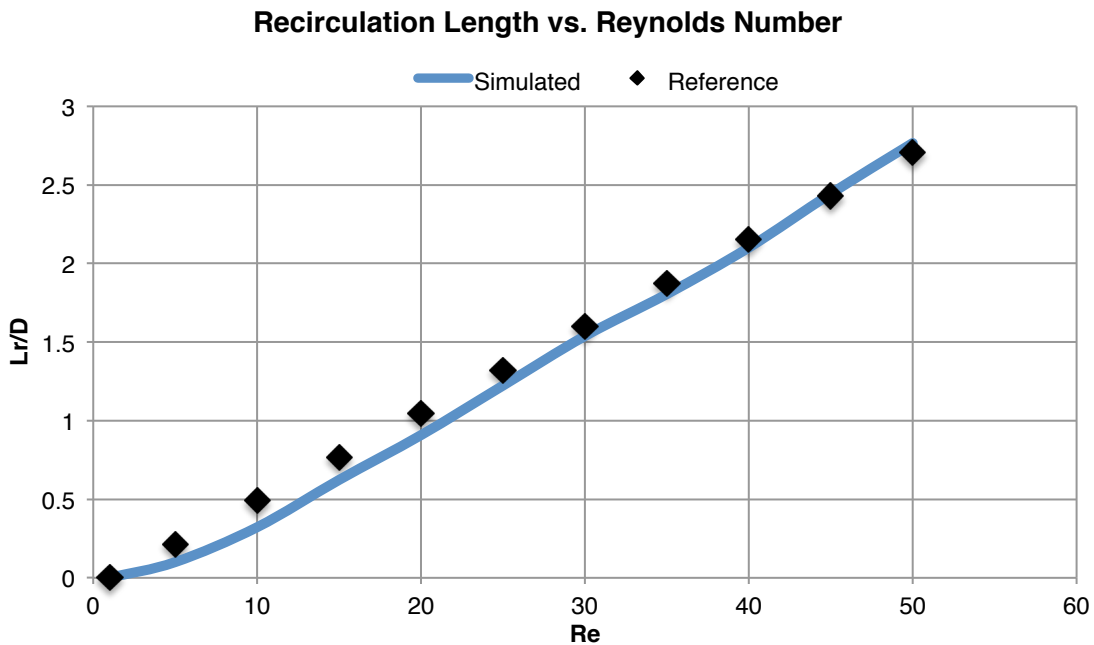


Figure 4.4: Dimensionless recirculation length vs. Reynolds number

In this situation the flow is completely symmetric respect to x-axis and the obstacle is only supporting an external load in the streamwise direction because the lift is 0 and the unique force component that is acting is the drag. As it can be seen in Figure 4.5, drag coefficient decreases with Reynolds number in these regimes as a consequence of the lower viscosity of the fluid and the same happens to viscous stresses. Reference values from [28].

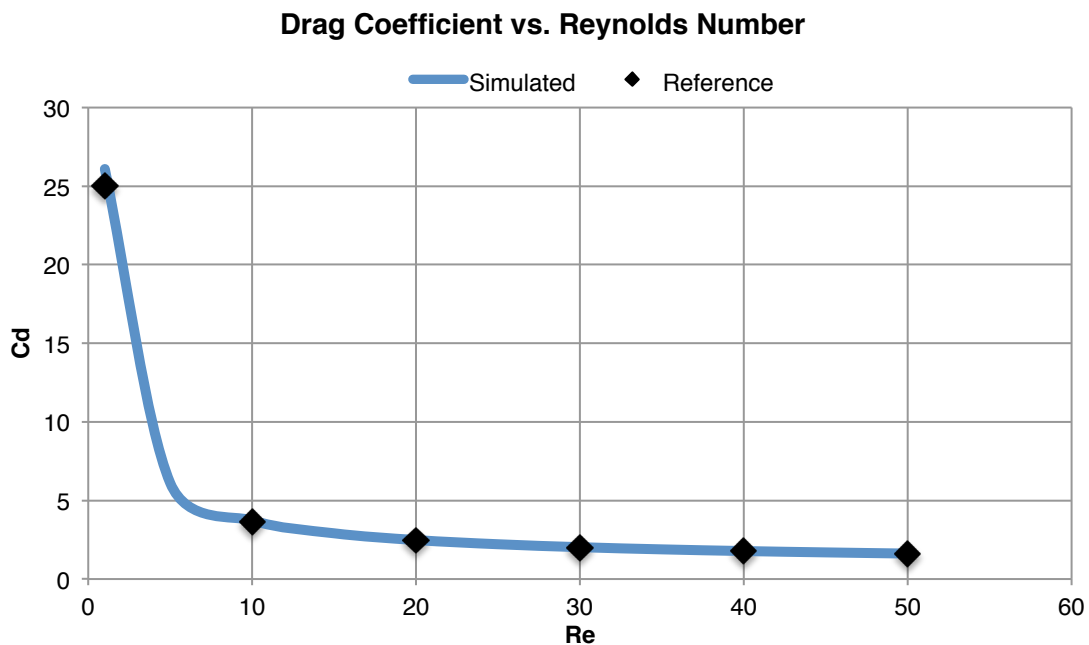


Figure 4.5 C_d vs Re for steady regimes

4.4.2 Unsteady flow

Above a critical Reynolds number that for this case is around $Re=60$, the flow becomes to be unsteady and a periodic oscillation appears downstream. This fact can be clearly seen in Figure 4.6 and Figure 4.7 where the Reynolds number in both images is the same but the time is different. The streamlines show that the flow is not steady and changes in time.

The same happens to the aerodynamic coefficients; those that were constant for lower Reynolds numbers now present the same periodic behaviour and, as a consequence, the force that the obstacle is supporting is also periodic (see Figure 4.9).

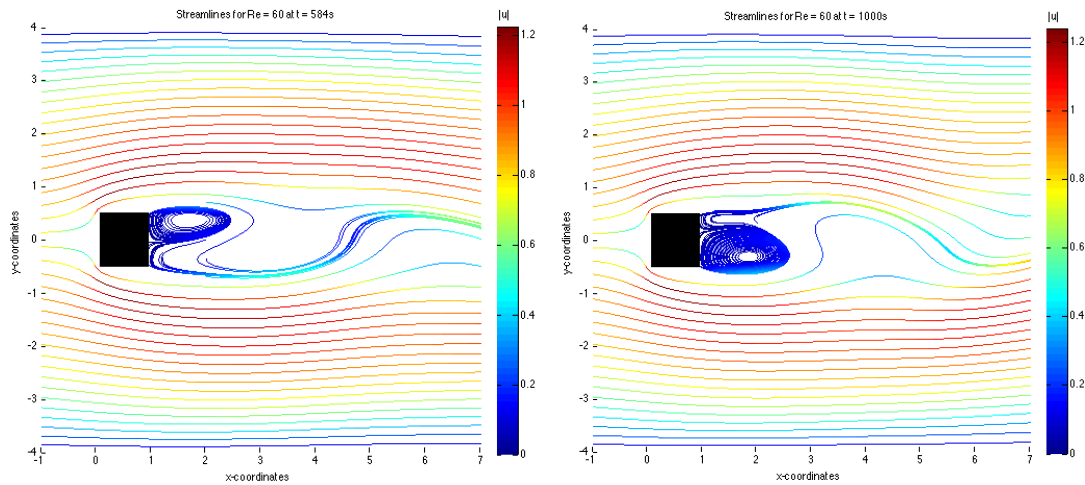


Figure 4.6: Streamlines for $Re=60$ at $t=584s$ (left) and $t=1000s$ (right)

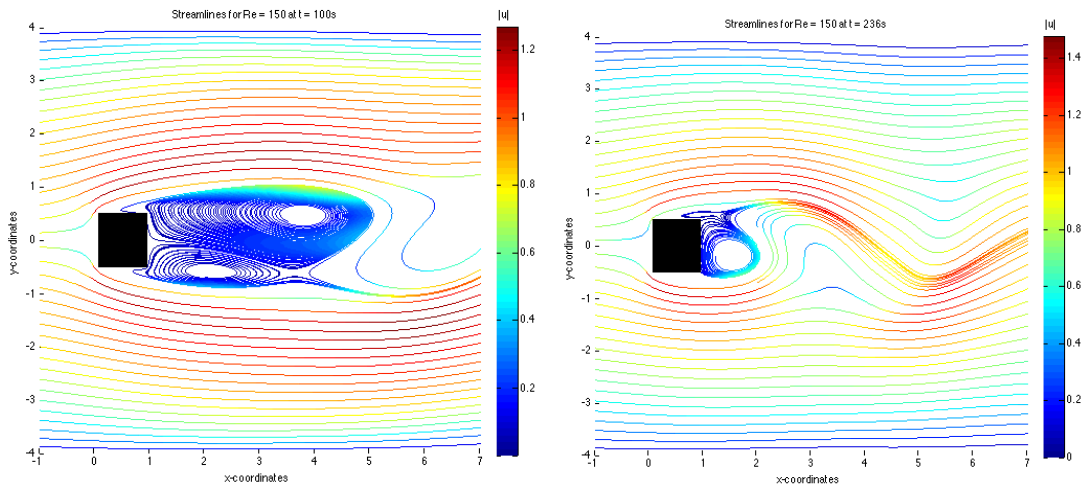


Figure 4.7: Streamlines for $Re=150$ at $t=100s$ (left) and $t=236s$ (right)

The responsible for this unsteady flow are the low-pressure vortex that detach from the obstacle and travel downstream that can be seen graphically in Figure 4.8.

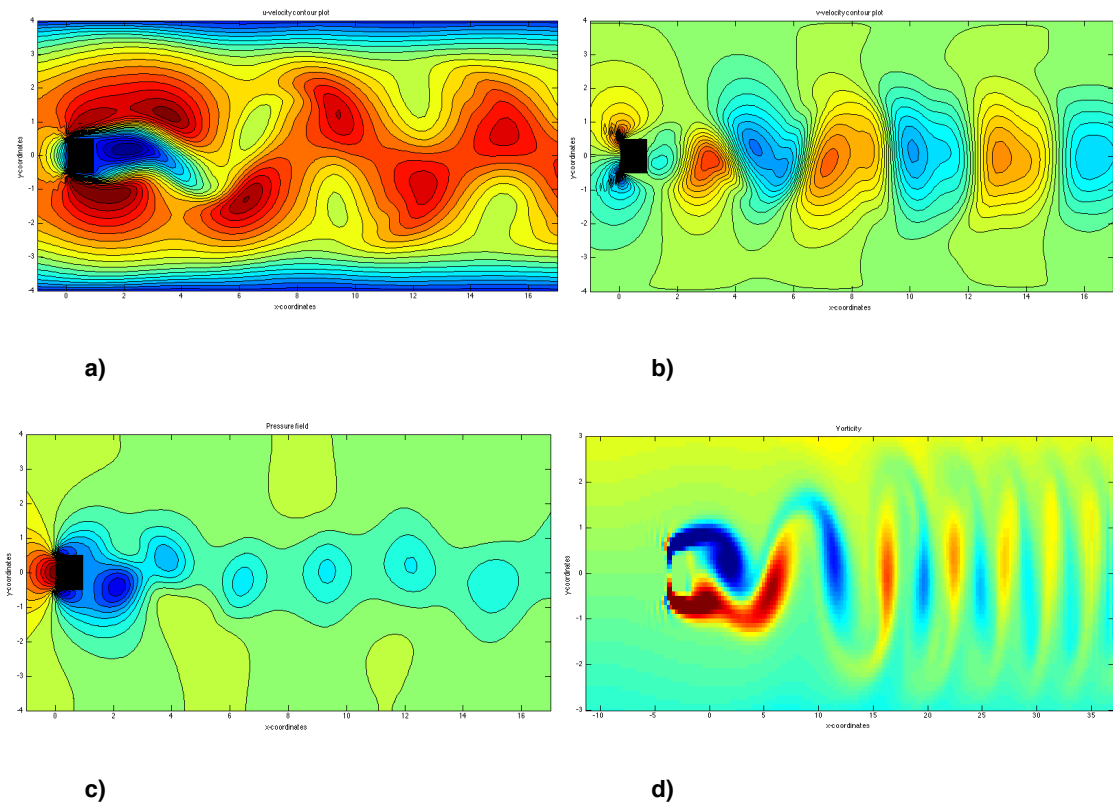


Figure 4.8: Downstream vortex visualization for $Re=100$ a) u -velocity b) v -velocity c) pressure d) vorticity

These four plots give a clear idea of what is happening downstream of the obstacle like the low-pressure zones that appear in the centre of the vortices in Figure 4.8 c) or the periodic pattern showed by the two components of the velocity. Additional graphic information can be found in ANNEX A SECTIONS 3.7 to 3.12.

The effect that this vortices have on the aerodynamic coefficients can be seen in the following plots.

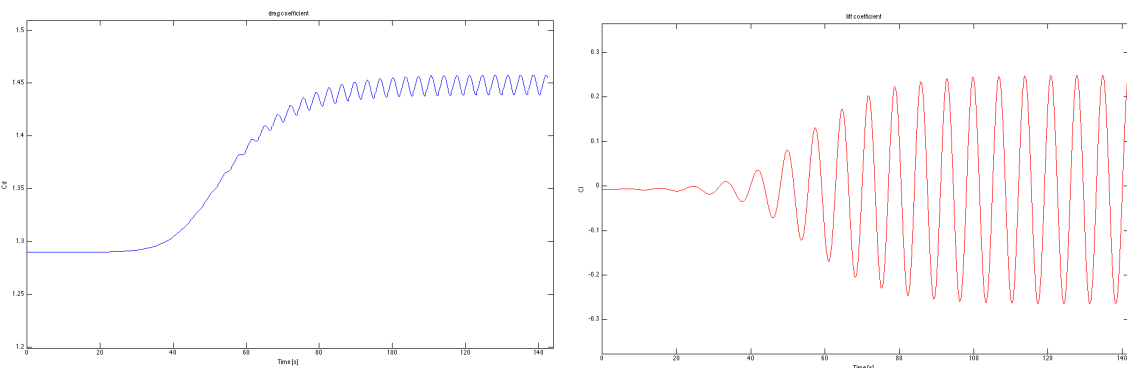


Figure 4.9: Periodic behavior of the aerodynamic coefficients for $Re = 100$

Notice that there are some differences between the two coefficients. As it has been explained, due to its symmetry the obstacle does not produce any lift and for steady regimes, a fact that was represented by a constant null lift coefficient. Above the critical

Reynolds value, the average lift coefficient remains 0 but presenting a noticeable oscillation.

The same happens to the drag coefficient. In Figure 4.9 it can be seen that after a certain time the periodic oscillation appears. The value of the drag coefficient oscillates around a value that is different of 0, so there is constant force pushing back the object along with the induced vibration. Reference values from [27].

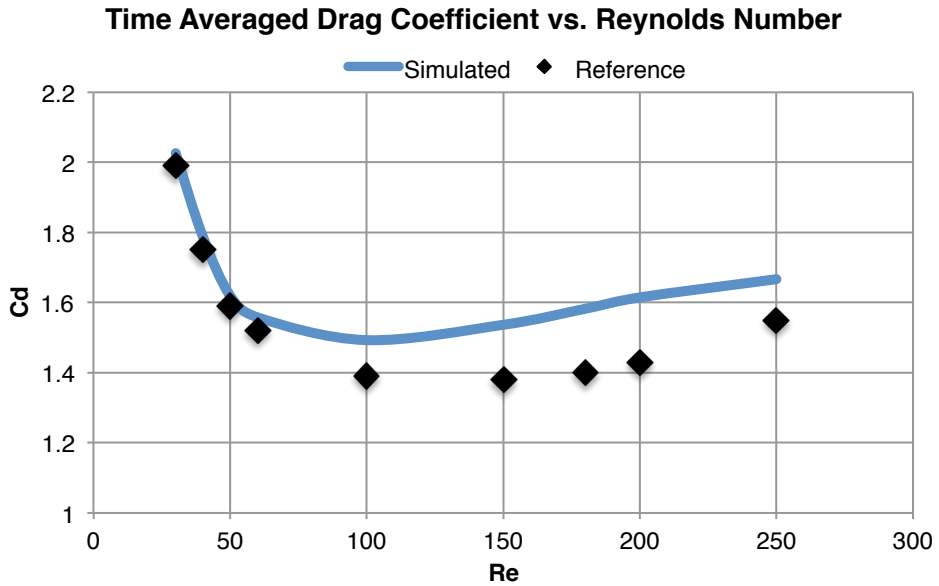


Figure 4.10: Time averaged drag coefficient vs. Reynolds number

The drag coefficient presents a very different behaviour in these regimes respect from the presented for the steady-state regimes. The viscous effects, or *viscous drag*, become less important as the Reynolds increases and so the total drag force is reduced. However, the detached flow behind the object creates a low-pressure zone that pushes it backwards and as it has been seen in Figure 4.4 that this region becomes bigger for higher Reynolds values. At a certain point, that in this case is placed between $Re=100$ and $Re=150$, the pressure difference is strong enough to change the decreasing tendency of the drag coefficient and the *pressure drag* becomes the larger contribution to the drag force.

Another observable difference between the two coefficients is that the force acting in the cross-stream direction presents much bigger oscillation amplitude (about ten times) than the amplitude of the force acting in the streamwise direction (see Figure 4.11 and Figure 4.12). This means that the structure not only has to deal with a more or less constant force in the parallel direction to the flux but also to induced vibrations that will have further affection in the perpendicular direction. It is known that these induced vibrations have an incredible destructive power if the structure enters in resonance so the designers must take this fact into account.

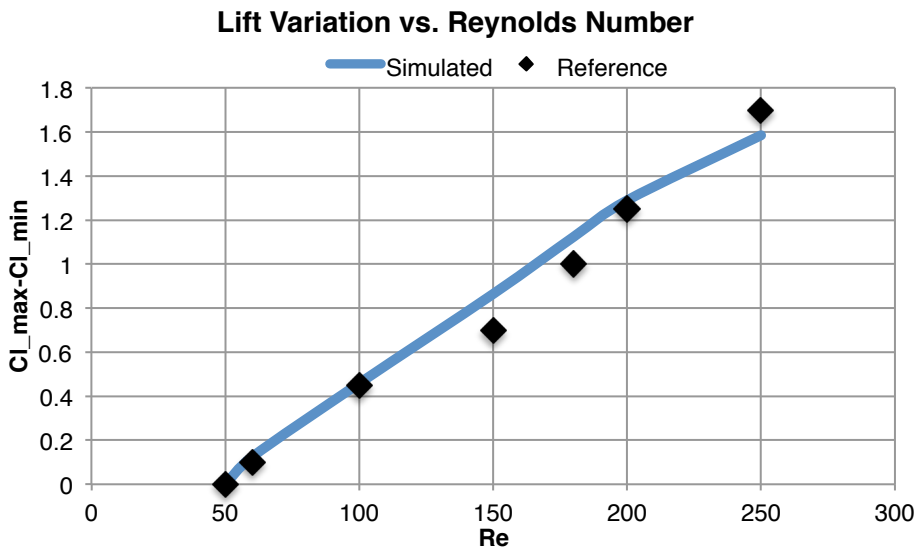


Figure 4.11: Lift variation vs. Reynolds number

The amplitude of the oscillation follows a clear growing tendency with the Reynolds number so more turbulent regimes will induce higher loads on the structure.

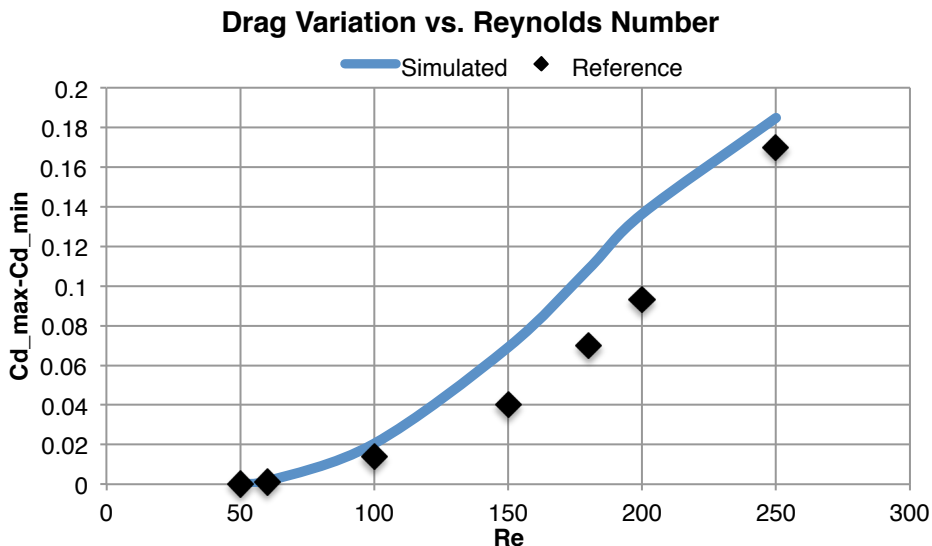


Figure 4.12: Drag variation vs. Reynolds number

Regarding the frequency of the induced vibrations, the Strouhal number has been calculated for different Reynolds regimes. To do so the time-evolution of the lift coefficient has been analysed using a discrete Fast Fourier Transformation [29]. The frequency of the phenomenon has a very specific value as it is seen Figure 4.9, where the coefficient almost fits a perfect sinusoidal curve. This fact creates an important peak in the frequency spectrum centred in the characteristic frequency of the phenomenon that can be easily identified. The evolution of the Strouhal with the Reynolds number can be seen in Figure 4.13.

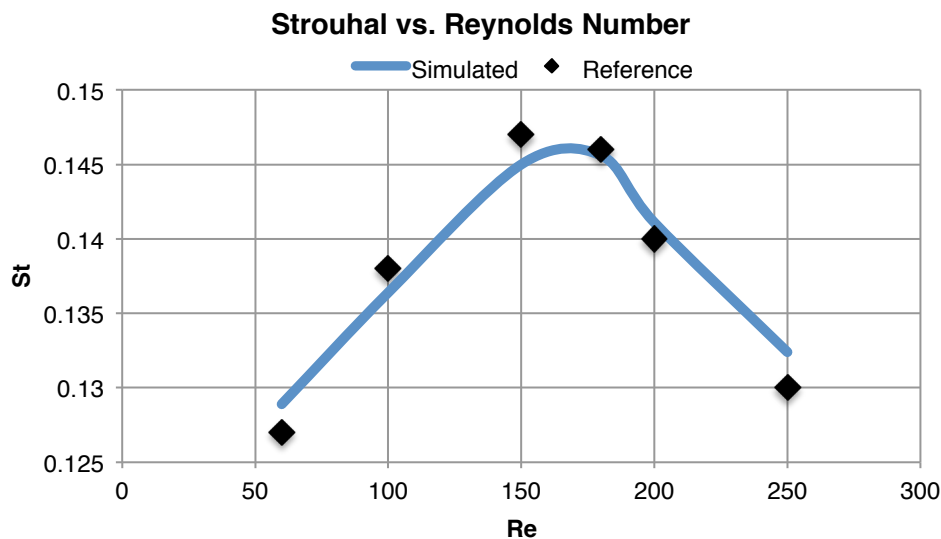


Figure 4.13: Strouhal vs. Reynolds number

Notice that for a given geometry and a fixed free stream velocity, the frequency of the phenomenon has a maximum around $Re=170$.

The Strouhal number is very useful to know which are the critical frequencies that the flow will induce to any structure that is placed into a stream and to design it in the proper way to avoid that natural frequency of the structure matches the one induced by the flow. As it is a dimensionless number, these values are valid for any square geometry regardless of its size.

4.4.3 Commentary on the obtained results

As it can be seen in the previous pages, the results obtained for steady regimes match almost perfectly the reference values while there are some differences in the results for the unsteady regimes.

In first place, the reference values were obtained using a FVM mesh of at least 500×80 elements, which is 2,5 times bigger than the one used in this study with 200×80 elements. The reason for using this coarser mesh is obviously the limited computational power and time available.

Nevertheless, both solutions follow the same tendency and the results obtained with the self-developed code would probably be improved using a denser mesh. It also has to be said that there exist little variations on the results between different references as the boundary conditions used have a certain implication in the obtained values.

5 Conclusions and future lines

5.1 Conclusions

The computational resources used in the development of this study are far beyond what is considered as state-of-the-art computing. In CFD computer power is always a limitation, even for the most advanced researchers.

In this case the limitation was set by the use of personal computer only with a single processor that has nothing to do compared with the supercomputers or clusters with hundreds or thousands of CPU's that are used in more advanced investigations. Furthermore, a professional researcher has vast experience and *know-how* in using these techniques that have nothing to do with the ones of an undergraduate student. This fact is reflected for example on the second-order numerical schemes used, which are quite simple compared to the fourth or eighth-order approximations that are used in some simulations.

However, performing state-of-the-art simulations was not the main goal of this project and from the first moment the limitations were taken into account and the scope was adapted having this fact in mind.

The software developed has demonstrated to be capable of solving the Navier-Stokes and heat transfer equations for incompressible laminar flows. The good results obtained from the benchmark cases are the proof of this fact.

A part from the simpler benchmark cases, another case of engineering interest has been tested. The conditions of this last simulation involved dealing with an open system and with an immersed object, a fact that adds certain difficulty and represent a closer approach to real applications of CFD.

Regarding this last point, this software in the actual point of development has very little application out of academic purposes as the regimes simulated involve very low velocities and simple geometries. However, this was in fact the main goal of the study: to set a basis from which develop more complicated applications and in that direction, the goals that were set have been achieved.

5.2 Future lines

From the point of actual development the following steps are quite clear. The code is capable of working with 2D laminar flows so it can be improved to make it capable of solving 2D turbulent cases. This means to adapt the code and make some verification on the discretized operators to be sure that they fulfil different constraints related with the generation of kinetic energy that are very important when working with turbulent flows.

Once this is done the natural step is to jump to 3D geometries with periodic boundary conditions. Turbulence is by nature a three-dimensional phenomenon so being able to work with this type of geometries is crucial. Nevertheless, this step involves increasing several times the control volumes that are needed to solve the problem so the computational power required is also much higher. For this reason the implementation of more efficient solvers or parallelization has to be considered.

Until now, only direct numerical simulation (DNS) has been considered but to develop engineering applications this technique is too much expensive. The approach that is followed is to use turbulence models such as RANS or LES to perform the modelization of part or the whole turbulence phenomenon, so the inclusion of a turbulence model to the self-developed software is an interesting fact once this point is reached.

5.3 Environmental impact

The alternative of performing CFD studies is to test real prototypes in a laboratory using a wind tunnel. A wind tunnel is a very expensive complex infrastructure that requires much more energy to operate than a personal computer, which also needs electrical energy to operate but the power requirements are much less. So from this point of view the advantage of using computer simulations is clear.

Furthermore, the prototypes tested in a real wind tunnel have to be built, which can suppose quite a big amount of wasted material if different geometries are tested or the prototypes suffer any kind of damage.

References

- [1] AMWEL Enterprises, “A Brief History of CFD,” 2008. [Online]. Available: <http://www.amwel.com/history.html>. [Accessed: 03-Mar-2015].
- [2] Wikipedia Contributors, “History of Fluid Mechanics,” *Wikimedia Commons*, 2015. [Online]. Available: https://en.wikipedia.org/wiki/History_of_fluid_mechanics. [Accessed: 04-Mar-2015].
- [3] G. Biswas, “Historical Developments in Computational Fluid Dynamics (CFD),” 2000. [Online]. Available: http://www.iitk.ac.in/infocell/Archive/dirjan2/techno_cfd.html. [Accessed: 03-Mar-2015].
- [4] Centrum Wiskunde & Informatica, “History of Theoretical Fluid Dynamics.” [Online]. Available: <http://www.cwi.nl/fluiddynamicshistory>. [Accessed: 05-Mar-2015].
- [5] Wikipedia Contributors, “Computational Fluid Dynamics,” 2015. [Online]. Available: https://en.wikipedia.org/wiki/Computational_fluid_dynamics. [Accessed: 04-Mar-2015].
- [6] A. J. Chorin and J. E. Marsden, *A Mathematical Introduction to Fluid Mechanics*. New York, NY: Springer US, 1979.
- [7] R. J. Leveque, *Finite-Volume Methods for Hyperbolic Problems*. Cape Town: Cambridge University Press, 2002.
- [8] Centre Tecnològic de Transferència de Calor, “Numerical Solution of Convection.”
- [9] C. Schär, “The Courant-Friedrichs-Levy (CFL) Stability Criterion Interpretation of Courant number,” pp. 1–7.
- [10] Centre Tecnològic de Transferència de Calor, “Introduction to the Fractional Step Method,” pp. 1–10.
- [11] United States Department of Transportation, “CHAPTER 5: Grid Generation.” [Online]. Available: <http://ntl.bts.gov/DOCS/ch5.html>. [Accessed: 10-Jun-2015].
- [12] S. V. Patankar, *Numerical heat transfer and fluid flow*. New York, NY: Hemisphere Publishing Corporation, 1980.
- [13] Wikipedia Contributors, “Gauss-Seidel Method,” 2015. [Online]. Available: http://en.wikipedia.org/wiki/Gauss–Seidel_method. [Accessed: 24-Feb-2015].

- [14] Wikipedia Contributors, “Tridiagonal Matrix Algorithm,” 2015. [Online]. Available: http://en.wikipedia.org/wiki/Tridiagonal_matrix_algorithm. [Accessed: 25-Feb-2015].
- [15] F. X. Trias, “Direct numerical simulation and regularization modelling of turbulent flows on loosely coupled parallel computers using symmetry-preserving discretizations,” Universitat Politècnica de Catalunya, 2006.
- [16] Centre Tecnològic de Transferència de Calor, “A Two-dimensional Steady Convection-Diffusion Equation: the Smith-Hutton problem,” 2015.
- [17] U. Ghia, K. Ghia, and C. Shin, “High-Re solutions for incompressible flow using the Navier-Stokes equations and a multigrid method,” *J. Comput. Phys.*, vol. 411, pp. 387–411, 1982.
- [18] Centre Tecnològic de Transferència de Calor, “Course on Numerical Methods in Heat Transfer and Fluid Dynamics. Unit 4: Fractional Step Method [Powerpoint Slides].”
- [19] G. de Vahl Davis, “Natural convection of air in a square cavity: a bench mark numerical solution,” ... *J. Numer. methods fluids*, vol. 3, no. July 1982, pp. 249–264, 1983.
- [20] G. de Vahl Davis and I. P. Jones, “Natural convection in a square cavity: a comparison exercise,” *Int. J. Numer. Methods Fluids*, vol. 3, no. July 1982, pp. 227–248, 1983.
- [21] F. X. Trias, a. Gorobets, M. Soria, and a. Oliva, “Direct numerical simulation of a differentially heated cavity of aspect ratio 4 with Rayleigh numbers up to 1011 - Part I: Numerical methods and time-averaged flow,” *Int. J. Heat Mass Transf.*, vol. 53, no. 4, pp. 665–673, 2010.
- [22] F. Dabbagh, “Direct numerical simulation of laminar and turbulent Rayleigh-Bénard convection,” Universitat Politècnica de Catalunya, 2013.
- [23] D. C. Wan, B. S. V Patnaik, and G. W. Wei, “A New Benchmark Quality Solution for the Buoyancy-Driven Cavity by Discrete Singular Convolution,” *Numer. Heat Transf.*, no. March, 2001.
- [24] A. Sohankar, C. Norberg, and L. Davidson, “Low-Reynolds-number flow around a square cylinder at incidence: Study of blockage, onset of vortex shedding and outlet boundary condition,” *Doktorsavhandlingar vid Chalmers Tek. Högsk.*, vol. 26, no. 1371, pp. 39–56, 1998.
- [25] A. H. Techet, “13.42 Lecture: Vortex Induced Vibration.” [Online]. Available: http://ocw.mit.edu/courses/mechanical-engineering/2-22-design-principles-for-ocean-vehicles-13-42-spring-2005/readings/lec20_viv1.pdf [Accessed: 25-May-2015]

- [26] J. Meseguer Ruiz and A. Sanz Andrés, *Aerodinámica Básica*, 2nd ed. Madrid: Ibergarceta Publicaciones, 2011.
- [27] M. Bruer, J. Bernsdorf, and D. Zeiser, “Accurate computations of the laminar flow past a square cylinder based on two different methods: lattice-Boltzmann and finite-volume,” *Int. J. Heat Fluid Flow*, vol. M, pp. 186–196, 2000.
- [28] A. K. Dhiman, R. P. Chhabra, and V. Eswaran, “Flow and heat transfer across a confined square cylinder in the steady flow regime: Effect of Peclet number,” *Int. J. Heat Mass Transf.*, vol. 48, no. 21–22, pp. 4598–4614, 2005.
- [29] The Mathworks Inc., “Fast Fourier Transform,” 2015. [Online]. Available: <http://es.mathworks.com/help/matlab/ref/fft.html>. [Accessed: 25-May-2015].

